FAR-IR/SUBMILLIMETER SPECTROSCOPIC COSMOLOGICAL SURVEYS:
PREDICTIONS OF INFRARED LINE LUMINOSITY FUNCTIONS FOR z<4 GALAXIES

Luigi Spinoglio[1], Kalliopi M. Dasyra[2,3], Alberto Franceschini[4], Carlotta Gruppioni[5], Elisabetta Valiante[6]
and Kate Isaak[7]
Draft version October 24, 2011

ABSTRACT

Star formation and accretion onto supermassive black holes in the nuclei of galaxies are the two most energetic processes in the Universe, producing the bulk of the observed emission throughout its history. We simulated the luminosity functions of star-forming and active galaxies for spectral lines that are thought to be good spectroscopic tracers of either phenomenon, as a function of redshift. We focused on the infrared (IR) and sub-millimeter domains, where the effects of dust obscuration are minimal. Using three different and independent theoretical models for galaxy formation and evolution, constrained by multi-wavelength luminosity functions, we computed the number of star-forming and active galaxies per IR luminosity and redshift bin. We converted the continuum luminosity counts into spectral line counts using relationships that we calibrated on mid- and far-IR spectroscopic surveys of galaxies in the local universe. Our results demonstrate that future facilities optimized for survey-mode observations, i.e., the Space Infrared Telescope for Cosmology and Astrophysics (SPICA) and the Cerro Chajnantor Atacama Telescope (CCAT), will be able to observe thousands of $z>1$ galaxies in key fine-structure lines, e.g., [Si II], [O I], [O III], [C II], in a half-square-degree survey, with one hour integration time per field of view. Fainter lines such as [O IV], [Ne V] and H$_2$ (0-0)S1 will be observed in several tens of bright galaxies at $1 < z < 2$, while diagnostic diagrams of active-nucleus vs star-formation activity will be feasible even for normal $z\sim1$ galaxies. We discuss the new parameter space that these future telescopes will cover and that strongly motivate their construction.

Subject headings: Galaxies: evolution, active, starburst, Seyfert - Techniques: imaging spectroscopy

1. INTRODUCTION

Tremendous progress in infrared (IR) astronomy was made in the last decade, largely driven by the launch of the *Spitzer* and *Herschel* space telescopes. Nonetheless, several basic questions remain unanswered in the fields of observational cosmology and galaxy formation and evolution, emphasizing the need for future missions. These regard our incomplete knowledge on how the primordial gas collapses to form new stars, on the different modes of star formation, and on the potentially coeval growth of black holes and galaxies. Below, we elaborate on each of these turn. We argue that fine-structure and molecular lines observable in IR lines can help us address them, and we present a set of simulations that support the need for future survey-oriented facilities that can make a strong impact on studies of galaxy evolution.

The collapse of the primordial gas at very high redshifts that led to the formation of the first stars and galaxies is thought to have occured via H$_2$ line emission, which acts

[1] Istituto di Fisica dello Spazio Interplanetario, INAF, Via Fosso del Cavaliere 100, I-00133 Roma, Italy
Electronic address: luigi.spinoglio@ifsi-roma.inaf.it
[2] Laboratoire AIM, CEA/DSM-CNRS-Université Paris Diderot, Irfu/Service dAstrophysique, CEA Saclay, F-91191 Gif-sur-Yvette, France
[3] Observatoire de Paris, LERMA (CNRS:UMR8112), 61 Av. de l´ Observatoire, F-75014, Paris, France
[4] Dipartimento di Astronomia - Universitá di Padova, Vicolo dell´ Osservatorio 5, 35122 Padova, Italy
[5] Osservatorio Astronomico di Bologna - INAF, Via Ranzani 1, 40127, Bologna, Italy
[6] Department of Physics and Astronomy, University of British Columbia, 6224 Agricultural Road, Vancouver, BC V6T 1Z1
[7] ESA Research & Scientific Support Department - ESTEC, Keplerlaan 1, 2200 AG Noordwijk, The Netherlands

as a very effective cooling mechanism in low-metallicity and low- temperature ($<10^4$ K) environments (Wise & Abel 2007; Obreschkow & Rawlings 2009). Even though H$_2$ remains a main coolant soon after the epoch of reionization, the direct detection of H$_2$ gas at very high z is yet to be achieved observational point of view.

Recent studies of the global infrared continuum and molecular gas properties of galaxies in the local and intermediate/high redshift Universe suggest that mergers and non- or weakly-interacting star-forming galaxies follow two separate Kennicutt-Schmidt relations with similar exponents, but different normalizations (Genzel et al. 2010; Daddi et al. 2010; Gracia-Carpio et al. 2011). At high-z, both galaxy mergers and accretion of cold gas via cooling flows have been suggested as sufficient mechanisms to produce IR luminosities $>10^{12}$ $L_\odot$ (Powell et al. 2011), unlike in the local Universe where ultraluminous IR galaxies (ULIRGs) are predominantly associated with mergers of comparable mass spirals (Dasyra et al. 2006). The parameters that determine the mode of star formation and control its efficiency are not yet understood. While *Spitzer* and *Herschel* helped us to identify and determine the star-formation rates of ULIRGs at $z\lesssim3$, the bulk of star formation at these redshifts is thought to take place in galaxies of lower luminosity (Perez-Gonzalez et al. 2005; Reddy et al. 2010; Ly et al. 2011). Characterizing the star formation in such systems is essential for understanding the formation of present-day ellipticals and downsizing (Cowie et al. 1996).

Studies of local massive galaxies and theoretical models suggest that most spheroids host massive black holes (Richstone et al. 1998; Fabian 1999). The observed correlations between the masses of these black holes and the

luminosities and stellar velocity dispersions of their host galaxies (Kormendy & Richstone 1992; Magorrian et al. 1998; Ferrarese & Merrit 2000; Tremaine et al. 2002; Ferrarese & Ford 2000; Shankar et al. 2009; Gultekin et al. 2009) are remarkable, given the vastly different scales that they involve. The enormous difference between the black hole Schwarzschild radius and the characteristic radius of the bulge indicates that these relations possibly reflect the coeval formation of the two in a common gravitational potential. To date, this scenario has been primarily tested through the comparison of the star-formation rate vs the black hole accretion rate as a function of look-back time (Treu et al. 2004; Marconi et al. 2004; Merloni et al. 2004; Shim et al. 2009; Gruppioni et al. 2011). Indeed, both activities have been found to peak at comparable redshifts, between $z \sim 1$-3. To further unravel and understand the relationship between black hole growth and bulge formation we need to compare the shape of the mass functions of galaxies with those of actively accreting black holes (Dasyra et al. 2011). Mass estimates of black holes in obscured systems will be needed for this purpose.

The complex relationship between star formation and active galactic nucleus (AGN) activity, which could extend over long duty cycles (of a few hundreds of Myrs), constrains the quantities that can be used as pure diagnostics of either activity. Present cosmological surveys are hampered when it comes to disentangling AGN from starburst activity. For example, an unambiguous AGN indicator in the IR is the continuum emission from dust just below sublimation temperature in the AGN torus (Schweitzer et al. 2006; Mor et al. 2009; Mullaney et al. 2010). However, its detection is often uncertain. The use of a torus model to reproduce the observed spectral energy distribution (SED) of galaxies can depend on the choice of the star-forming galaxy template that is simultaneously used for the same purpose. Selecting high-z sources with unambiguous evidence for hot dust–that is independent of the chosen star-forming galaxy template–can lead to small, biased samples of luminous AGN. Less strict criteria can lead to incomplete AGN samples that are contaminated by starburst galaxies. This is frequently the case for AGN selected based on mid-IR color-color diagrams (Lacy et al. 2004; Stern et al. 2005; Barmby et al. 2006). The other unambiguous signature of a hard, AGN-related radiation field is the line emission from ionic species that require $\gtrsim$100eV for their creation. A line often used for this purpose is [NeV] at 14.32μm, which however was only seen in stacked spectra of $z \gtrsim 1$ galaxies with *Spitzer* (Dasyra et al. 2009).

Observing new FIR-selected galaxy samples, or sampling the peak of the IR SEDs of presently known samples, will not only enable us to address such open questions, but to also obtain a more coherent view of high-z galaxy populations. The thousands of 24μm -selected, IR-bright galaxies discovered by *Spitzer* (Papovich et al. 2004; Rigby et al. 2004; Fadda et al. 2004; LeFloc'h et al. 2004; Houck et al. 2005; Huang et al. 2009), the hundreds of mm galaxies (e.g. Smail et al. 1997; Hughes et al. 1998; Barger et al. 1998; Scott et al. 2002; Borys et al. 2003; Webb et al. 2003; Coppin et al. 2006), (e.g. Greve et al. 2004; Laurent et al. 2005; Scott et al. 2008; Perera et al. 2008; Austermann et al.

2010), the tens of thousands far-IR and sub-mm galaxies detected at high-redshifts by the *Herschel* observatory (e.g. Berta et al. 2010; Oliver et al. 2010), and the thousands of near IR dropouts (e.g. Caputi et al. 2005; Daddi et al. 2005; Papovich et al. 2006) known to date are often treated as physically disconnected populations.

Spectroscopic surveys with future missions or facilities will help us address the above-mentioned points. Expected to be at least one order of magnitude more sensitive than their predecessors, future spectrographs will observe ionic and molecular gas lines, in addition to the dust broadband features and their underlying continua, for large galaxy samples over wide fields of view. In the spirit of demonstrating what can be done in the future in the IR/submm domain in the field of galaxy evolution, we present simulations of the number of galaxies that will be observed in key IR lines and features at each z range with the SPace IR telescope for Cosmology and Astrophysics (SPICA) and the Cerro Chajnantor Atacama Telescope (CCAT). We focus on SPICA and CCAT as these are conceived to be large blind survey machines, unlike the James Webb Space Telescope (JWST) and the Atacama Large Millimeter Array (ALMA), that are optimized for deep single-source observations.

The paper is organized as follows. In Section 2 we present the simulations, and the physical assumptions that go into them, including the adopted line-to-bolometric luminosity conversion functions that we measured from observations of local galaxies. The main results of the simulations, i.e., the number of galaxies and AGN that can be detected for each ionized or molecular gas line with z for a given flux limit, are presented in Section 3, followed by a discussion in Section 4. Throughout the paper we will adopt the standard cosmological model with $\Omega_M = 0.27$, $\Omega_\Lambda = 0.73$, $H_0 = 71$ km s^{-1} Mpc^{-1}.

2. SIMULATING SPECTROSCOPIC SURVEYS IN THE IR

The computation of the number of objects that future missions will detect in each line was a two-fold process. First, we used three galaxy evolution models that are based on galaxy counts and luminosity functions in several bands of the *Spitzer*, AKARI and *Herschel* missions to predict the integrated 8-1000μm IR luminosity function at different z bins. We have considered three different models with the aim of basing our conclusions on solid results, and at the same time quantifying the range of the predictions. We then computed correlations between the IR luminosity and the luminosities of various fine-structure lines, molecular lines, and dust emission features, using samples of local galaxies with complete mid- and far-IR spectroscopic coverage. This enabled us to transform the continuum luminosity functions into line luminosity functions up to $z < 4$ and compute the line detection rates.

2.1. *Predicting continuum luminosity functions with the Franceschini et al. (2010) model*

As a first approach, we adopted the model developed by Franceschini et al. (2010). This is a backward evolution model that fits essentially all available data from *Spitzer*, ISO, COBE, and SCUBA. Moreover, it includes constraints from preliminary results of the *Herschel Space Observatory* surveys (presented in the Science Demonstration Phase papers of Oliver et al. 2010;
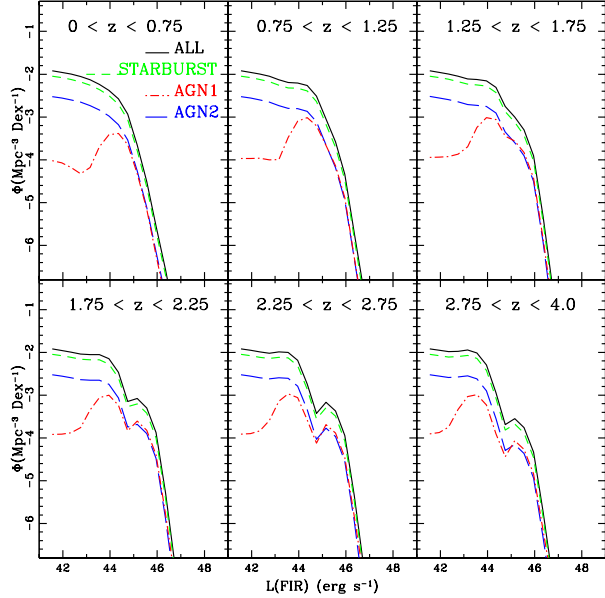
FIG. 1.— IR (8−1000 μm) continuum luminosity function constructed from the Franceschini et al. (2010) model.

Berta et al. 2010; Glenn et al. 2010; Gruppioni et al. 2010; Nguyen et al. 2010).

The model accounts separately for normal spiral galaxies, actively star-forming galaxies, and for type 1 and 2 AGNs. The actively star-forming population is further split into two galaxy classes, i.e., moderate-luminosity luminous infrared galaxies (LIRGs) and high-luminosity ULIRGs. The LIRGs have typical IR luminosities $\simeq 10^{11} L_{\odot}$ and the ULIRGs $\simeq 10^{12} L_{\odot}$. They are treated as two galaxy classes, with different luminosity functions, evolution rates, and spatial clustering properties.

The broad-line AGNs–type 1 Seyferts and quasars– were modelled adopting luminosity functions and evolution rates consistent with those observed in optical and mid-IR surveys (e.g. Rush, Malkan & Spinoglio 1993; Spinoglio et al. 1995). As detailed in Franceschini et al. (2010), important constraints on the infrared evolution properties of type 1 AGNs have been inferred from a flux-limited sample of 24μm-selected sources with complete spectroscopic classification, as reported by Rodighiero et al. (2010). These objects are easily identified by their flat spectral shapes over the optical through IR wavelength range (Spinoglio, Andreani & Malkan 2002).

Narrow-line type 2 AGNs are instead much more difficult to disentangle from starburst galaxies. Therefore their statistical properties and incidence among the IR population at high redshifts are still essentially unknown. At the present stage of knowledge, the model simply considers type 2 AGNs as a fraction of both low-luminosity and high-luminosity starbursts. In an attempt to constrain such fractions, a follow-up analysis by Franceschini et al. (2011, in preparation) has compared the star-formation and stellar-mass assembly histories of galaxies, and found that the two are consistent with each other if 10% of the LIRG and 30% of the ULIRG objects are dominated by obscured (type 2) AGN accretion. These

are the fractional contributions for type 2 AGNs adopted in the present work. It is clear from the above that this modelling might easily give results inconsistent with the value derived from both predictions by the AGN unification scheme and observations (e.g., from the SLOAN and FIRST surveys, Lu et al. 2010) of a ∼1 to 3 ratio of type-1 to type 2 objects. Indeed, the validity of the AGN unification at high redshifts has never been proven in detail, and will be one of the major outcomes of futures spectroscopic surveys in the IR.

Figure 1 shows the continuum far-IR luminosity functions for all populations in each z range considered: 0.<z<0.75, 0.75<z<1.25, 1.25<z<1.75, 1.75<z<2.25, 2.25<z<2.75 and 2.75<z<4.0.
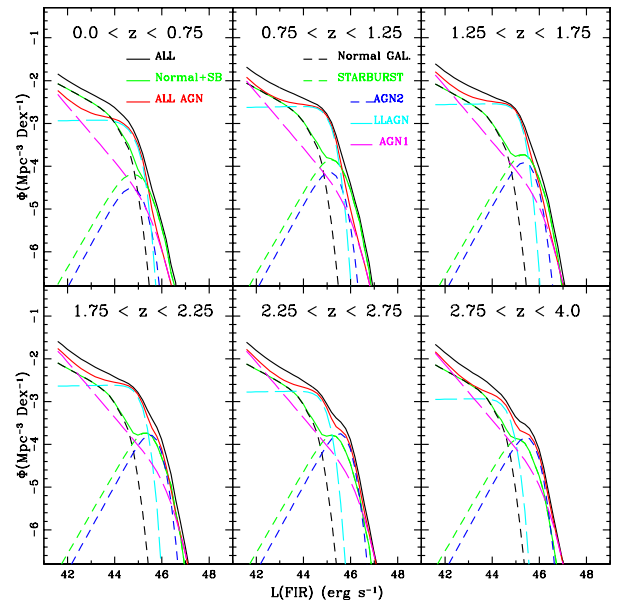

FIG. 2.— IR luminosity function from Gruppioni et al. (2011) for various galaxy populations, i.e., normal and starburst galaxies, low luminosity AGN, type 1 AGN and type 2 AGN.

2.2. Predicting continuum luminosity functions with the Gruppioni et al. (2011) model

Gruppioni et al. (2011) have also developed a backward evolution model fitting the main constraints provided by IR/sub-mm surveys in the 15μm to 500μm range. In the mid-IR (MIR), it uses data from both ISO and *Spitzer* that are available in the literature, at 15μm from the ELAIS-S1 (Gruppioni et al. 2002), HDF-N, HDF-S and Marano fields (Elbaz et al. 1999), ultradeep lensed (Metcalfe et al. 2003), Lockman Deep and Shallow (Rodighiero et al. 2004), and at 24μm from the GOODS (Papovich et al. 2004) and SWIRE surveys (Shupe et al. 2008). In the FIR, we use data from *Herschel*, including those of the very recent PACS Evolutionary Probe Survey (Berta et al. 2010; Gruppioni et al. 2010), the *Herschel*-ATLAS Survey (Eales et al. 2010; Clements et al. 2010), and the *Herschel* Multi-tiered Extra-galactic Survey (Oliver et al. 2010; Vaccari et al. 2010). The model uses the classical approach of evolving a local luminosity function in luminosity and/or density with z, with a different evolutionary

description for galaxies and AGN. What differentiates this model from others is the spectral energy distribution (SED) scheme that it uses to distinguish between the different IR-bright galaxy populations. The scheme is based on a large spectroscopic study of MIR-selected sources (Gruppioni et al. 2008), and it divides sources into five (instead of four) broad SED classes. These are the normal spiral galaxies, the starburst galaxies, the obscured type 2 AGNs, the unobscured type 1 AGNs, and the objects containing a low luminosity (LL) AGN. In other words, the authors of this model have put particular emphasis on determining the AGN contribution at low luminosities at all redshifts. The contribution of the various galaxy populations to the IR luminosity function can be seen in Figure 2.
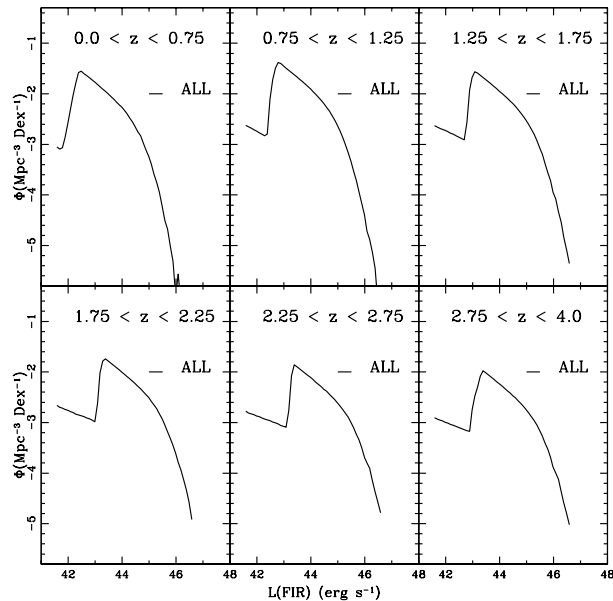

FIG. 3.— IR luminosity function from Valiante et al. (2009).

2.3. Predicting continuum luminosity functions with the Valiante et al. (2009) model

The third model that we used is the backward evolution model of Valiante et al. (2009). It was developed using *Spitzer* and SCUBA observations, and it has been very successful in predicting *Herschel* results (Berta et al. 2010; Altieri et al. 2010; Glenn et al. 2010; Oliver et al. 2010). This model allows us to take into account galaxies that are not 'pure' starburst or 'pure' AGN, and for which the ratio between IR lines might not be the ones expected assuming 'pure' SEDs. This is because the model considers all infrared galaxies as a single population, assuming that starbursts and AGN coexist. It then uses an empirical relation to assign to each galaxy the fraction of the IR luminosity that is powered by the AGN for its given luminosity and redshift. This relation was derived using a complete sample of local IRAS galaxies, and extrapolated to high z using *Spitzer* and SCUBA observations. Figure 3 shows the IR luminosity function predicted by this model for each z bin.
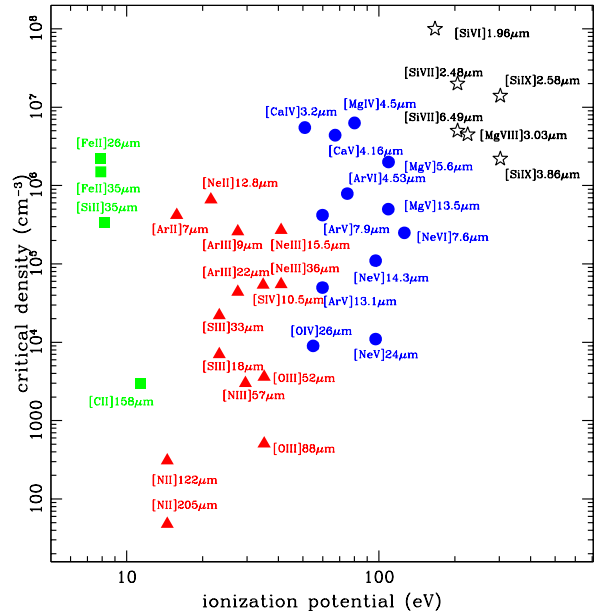

FIG. 4.— Critical density for collisional de-excitation vs. ionization potential of IR fine-structure lines.

2.4. Converting continuum luminosity functions to line or feature luminosity functions.

The galaxy number counts per redshift and bolometric IR luminosity bin that are predicted by each model need to be converted into line luminosity functions, in order to estimate the number of objects that will be detectable in various lines, and to assess whether several of the open questions presented in Section 1 can be addressed. For this purpose, we derived correlations between line and continuum luminosities, including lines for which such correlations were not previously available in the literature, e.g., that of [SiII] for both AGN and star-forming galaxies. We examined the PAH feature at 11.25μm, the purely rotational H_2 (0-0)S1 line at 17.03μm, and the [NeII] 12.8μm, [NeV] 14.3μm, [NeIII] 15.5μm, [SIII] 18.7μm, [NeV] 24.3μm, [OIV] 26μm, [SiII] 34.8μm, [OIII] 52μm, [NIII] 57μm, [OI] 63μm, [OIII] 88μm, [NII] 121.90μm, [OI] 145.52μm, and [CII] 157.74μm fine-structure lines. These lines cover a wide parameter space of the critical density vs. ionization potential diagram (see Fig. 4), tracing different astrophysical conditions: from photodissociation regions, to stellar/HII regions, to the AGN and coronal line regions (Spinoglio & Malkan 1992). This makes the combination of their ratios useful for the creation of AGN vs star-formation diagnostic diagrams (e.g. Spinoglio & Malkan 1992; Genzel et al. 1998; Dale et al. 2006; Smith et al. 2007).

For lines at wavelengths shorter than 35μm, we used the complete, 12μm-selected sample of local Seyfert galaxies (Tommasin et al. 2008, 2010) and the Bernard-Salas et al. (2009) sample of starburst galaxies to calibrate the line luminosities to L_{IR}. These samples have been extensively observed in the MIR with the IRS spectrometer (Houck et al. 2004) onboard *Spitzer* (Werner et

al. 2004), and the *Spitzer* spectra have been reduced and analysed in a consistent way. For the starburst galaxies, we excluded all objects for which there was evidence for the presence of an AGN from the literature or from the detection of [NeV] (see Table 1 of Bernard-Salas et al. 2009). For the long- wavelength lines, we used the heterogeneous sample of local galaxies compiled by Brauher et al. (2008) containing all observations collected by the LWS spectrometer (Clegg et al. 1996) onboard ISO (Kessler et al. 1996). The IR luminosities of the galaxies of our sample have been computed from the IRAS fluxes, using the formula of L_{IR}[8] representing the total mid- and far-infrared luminosity (Sanders & Mirabel 1996). All luminosities are in units of 10^{41} erg s^{-1}.

Using least-squares fitting, we obtained the following relations for the Seyfert galaxies,

$$\log(L_{\mathrm{PAH}11.25}) = (0.95 \pm 0.07)\log(L_{IR}) - (2.60 \pm 0.21) \quad (1)$$

with $R = 0.87$, $n = 69$, $\chi^2 = 7.1$

$$\log(L_{[\mathrm{NeII}]12.81}) = (0.98 \pm 0.06)\log(L_{IR}) - (3.25 \pm 0.18) \quad (2)$$

with $R = 0.89$, $n = 87$, $\chi^2 = 8.8$

$$\log(L_{[\mathrm{NeV}]14.32}) = (0.94 \pm 0.08)\log(L_{IR}) - (3.43 \pm 0.25) \quad (3)$$

with $R = 0.81$, $n = 81$, $\chi^2 = 14.8$

$$\log(L_{[\mathrm{NeIII}]15.55}) = (0.95 \pm 0.07)\log(L_{IR}) - (3.18 \pm 0.24) \quad (4)$$

with $R = 0.82$, $n = 87$, $\chi^2 = 15.0$

$$\log(L_{(\mathrm{H_2})17.03}) = (0.97 \pm 0.05)\log(L_{IR}) - (3.79 \pm 0.15) \quad (5)$$

with $R = 0.92$, $n = 76$, $\chi^2 = 5.3$

$$\log(L_{[\mathrm{SIII}]18.71}) = (0.90 \pm 0.07)\log(L_{IR}) - (3.30 \pm 0.21) \quad (6)$$

with $R = 0.85$, $n = 70$, $\chi^2 = 7.7$

$$\log(L_{[\mathrm{NeV}]24.31}) = (0.98 \pm 0.08)\log(L_{IR}) - (3.45 \pm 0.24) \quad (7)$$

with $R = 0.84$, $n = 71$, $\chi^2 = 10.5$

$$\log(L_{[OIV]25.89}) = (0.88 \pm 0.08)\log(L_{IR}) - (2.66 \pm 0.25) \quad (8)$$

with $R = 0.79$, $n = 83$, $\chi^2 = 14.9$

$$\log(L_{[\mathrm{SIII}]33.48}) = (0.98 \pm 0.05)\log(L_{IR}) - (3.21 \pm 0.17) \quad (9)$$

with $R = 0.91$, $n = 75$, $\chi^2 = 5.7$

$$\log(L_{[\mathrm{SiII}]34.82}) = (1.03 \pm 0.06)\log(L_{IR}) - (3.14 \pm 0.20) \quad (10)$$

with $R = 0.89$, $n = 72$, $\chi^2 = 7.3$

where for each relation the Pearson coefficient R, the number of considered objects n and the computed χ^2 are given. For the starburst galaxies, the corresponding relations are:

$$\log(L_{\mathrm{PAH}11.25}) = (1.17 \pm 0.11)\log(L_{IR}) - (3.03 \pm 0.32) \quad (11)$$

with $R = 0.95$, $n = 14$, $\chi^2 = 1.4$

$$\log(L_{[\mathrm{NeII}]12.81}) = (1.17 \pm 0.14)\log(L_{IR}) - (3.65 \pm 0.40) \quad (12)$$

with $R = 0.93$, $n = 14$, $\chi^2 = 2.1$

$$\log(L_{[\mathrm{NeIII}]15.55}) = (1.33 \pm 0.18)\log(L_{IR}) - (4.85 \pm 0.52) \quad (13)$$

with $R = 0.90$, $n = 15$, $\chi^2 = 3.9$

$$\log(L_{(\mathrm{H_2})17.03}) = (1.28 \pm 0.14)\log(L_{IR}) - (5.10 \pm 0.42) \quad (14)$$

with $R = 0.93$, $n = 15$, $\chi^2 = 2.6$

$$\log(L_{[\mathrm{SIII}]18.71}) = (1.09 \pm 0.15)\log(L_{IR}) - (3.79 \pm 0.45) \quad (15)$$

with $R = 0.89$, $n = 15$, $\chi^2 = 3.0$

$$\log(L_{[OIV]25.89}) = (1.24 \pm 0.24)\log(L_{IR}) - (5.13 \pm 0.74) \quad (16)$$

with $R = 0.85$, $n = 12$, $\chi^2 = 1.6$

$$\log(L_{[\mathrm{SIII}]33.48}) = (1.09 \pm 0.10)\log(L_{IR}) - (3.35 \pm 0.29) \quad (17)$$

with $R = 0.95$, $n = 15$, $\chi^2 = 1.2$

$$\log(L_{[\mathrm{SiII}]34.82}) = (1.11 \pm 0.09)\log(L_{IR}) - (3.26 \pm 0.25) \quad (18)$$

with $R = 0.96$, $n = 15$, $\chi^2 = 0.92$

The best-fit solution is shown in Figure 5 for each of the populations. Considering the sum of the populations, we derived the following generic relations:

$$\log(L_{\mathrm{PAH}11.25}) = (0.98 \pm 0.06)\log(L_{IR}) - (2.69 \pm 0.18) \quad (19)$$

with $R = 0.88$, $n = 83$ $\chi^2 = 9.4$

$$\log(L_{[\mathrm{NeII}]12.81}) = (0.99 \pm 0.06)\log(L_{IR}) - (3.26 \pm 0.20) \quad (20)$$

with $R = 0.84$, $n = 101$, $\chi^2 = 17.8$

$$\log(L_{[\mathrm{NeIII}]15.55}) = (1.10 \pm 0.07)\log(L_{IR}) - (3.72 \pm 0.23) \quad (21)$$

with $R = 0.83$, $n = 102$, $\chi^2 = 24.2$

$$\log(L_{(\mathrm{H_2})17.03}) = (1.07 \pm 0.05)\log(L_{IR}) - (4.19 \pm 0.16) \quad (22)$$

with $R = 0.91$, $n = 91$, $\chi^2 = 10.6$

$$\log(L_{[\mathrm{SIII}]18.71}) = (0.97 \pm 0.06)\log(L_{IR}) - (3.47 \pm 0.20) \quad (23)$$

with $R = 0.88$, $n = 70$, $\chi^2 = 7.9$

$$\log(L_{[OIV]25.89}) = (0.95 \pm 0.11)\log(L_{IR}) - (3.04 \pm 0.34) \quad (24)$$

with $R = 0.68$, $n = 95$, $\chi^2 = 36.6$

$$\log(L_{[\mathrm{SIII}]33.48}) = (0.99 \pm 0.05)\log(L_{IR}) - (3.21 \pm 0.14) \quad (25)$$

with $R = 0.92$, $n = 90$, $\chi^2 = 7.4$

$$\log(L_{[\mathrm{SiII}]34.82}) = (1.04 \pm 0.05)\log(L_{IR}) - (3.15 \pm 0.16) \quad (26)$$

with $R = 0.91$, $n = 87$, $\chi^2 = 8.4$

For the far-IR lines (Fig. 6), we obtain:

$$\log(L_{[OIII]51.81}) = (0.88 \pm 0.10)\log(L_{IR}) - (2.54 \pm 0.31) \quad (27)$$

with $R = 0.91$, $n = 16$, $\chi^2 = 2.6$

$$\log(L_{[\mathrm{NIII}]57.32}) = (0.78 \pm 0.10)\log(L_{IR}) - (2.58 \pm 0.32) \quad (28)$$

with $R = 0.94$, $n = 10$, $\chi^2 = 0.14$

$$\log(L_{[OI]63.18}) = (0.98 \pm 0.03)\log(L_{IR}) - (2.70 \pm 0.10) \quad (29)$$

with $R = 0.94$, $n = 109$, $\chi^2 = 9.1$

$$\log(L_{[OIII]88.36}) = (0.98 \pm 0.10)\log(L_{IR}) - (2.86 \pm 0.30) \quad (30)$$

with $R = 0.81$, $n = 55$, $\chi^2 = 12.7$

$$\log(L_{[\mathrm{NII}]121.9}) = (1.01 \pm 0.04)\log(L_{IR}) - (3.54 \pm 0.11) \quad (31)$$

with $R = 0.93$, $n = 100$, $\chi^2 = 13.3$

$$\log(L_{[OI]145.5}) = (0.89 \pm 0.06)\log(L_{IR}) - (3.55 \pm 0.17) \quad (32)$$

with $R = 0.91$, $n = 46$, $\chi^2 = 10.0$

$$\log(L_{[\mathrm{CII}]157.7}) = (0.89 \pm 0.03)\log(L_{IR}) - (2.44 \pm 0.07) \quad (33)$$

with $R = 0.92$, $n = 217$. $\chi^2 = 42.3$

---

[8] L_{IR} is computed by fitting a single-temperature dust emissivity model ($\epsilon \propto \nu^{-1}$) to the flux in all four IRAS bands, and should be accurate to $\pm5\%$ for dust temperatures in the range 25 - 65 K. We notice that the IR luminosities, as defined above, are model-dependent, and therefore could introduce some systematics. However these do not affect the derived relations, as they are within the given errors.
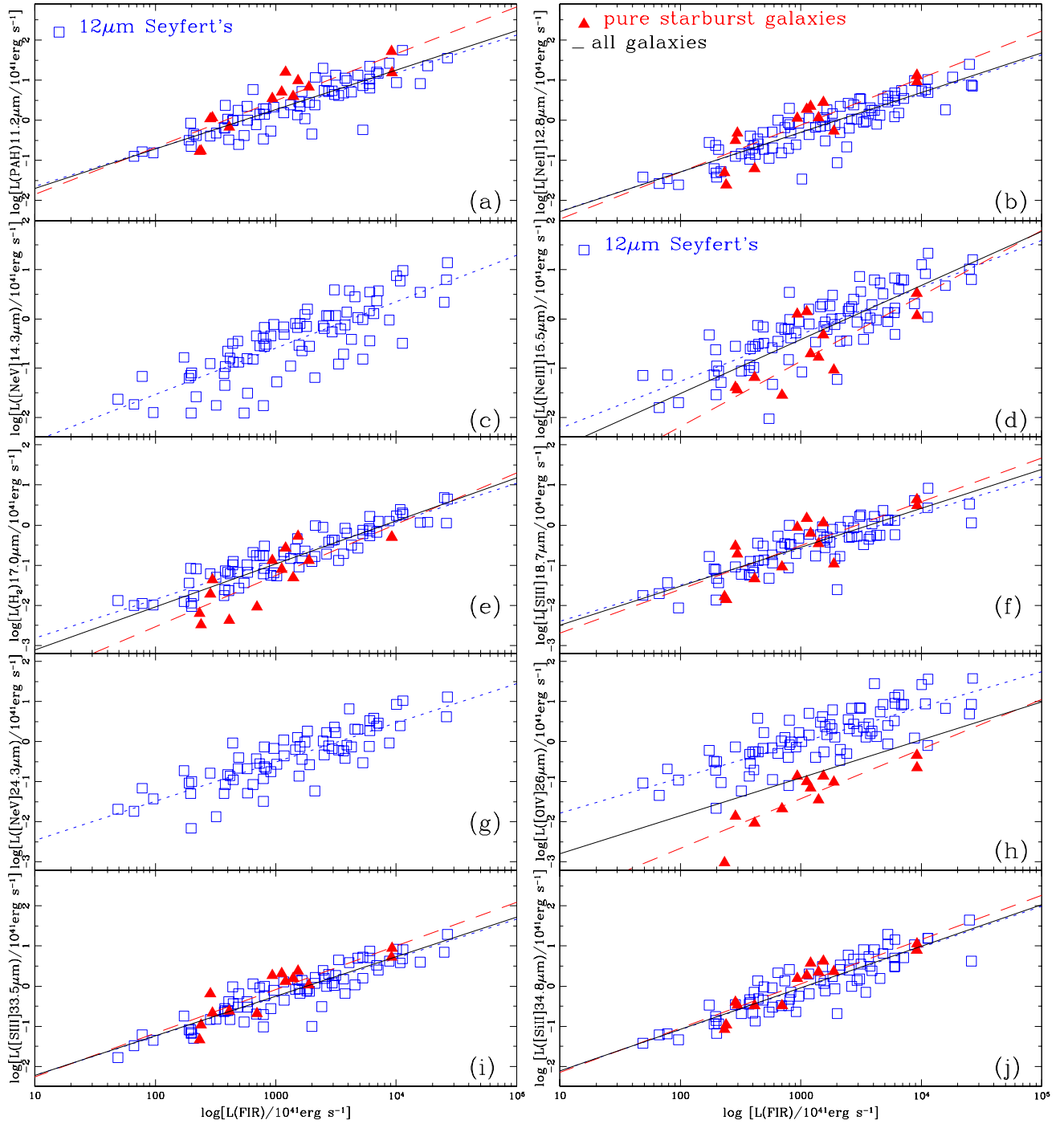
Fig. 5.— Correlations between the various feature and line luminosities and the far-IR luminosity for the Seyfert galaxies of the complete 12μm galaxy sample (Tommasin et al. 2008, 2010), and for the pure starburst galaxies of the sample of Bernard-Salas et al. (2009). The dotted, broken and solid lines represent the least-squares fit of the data of the Seyfert, the pure starburst galaxies and all galaxies populations together, respectively. Figures (c) and (g) have only the Seyfert galaxies, because the [NeV] lines are not detected in starburst galaxies.
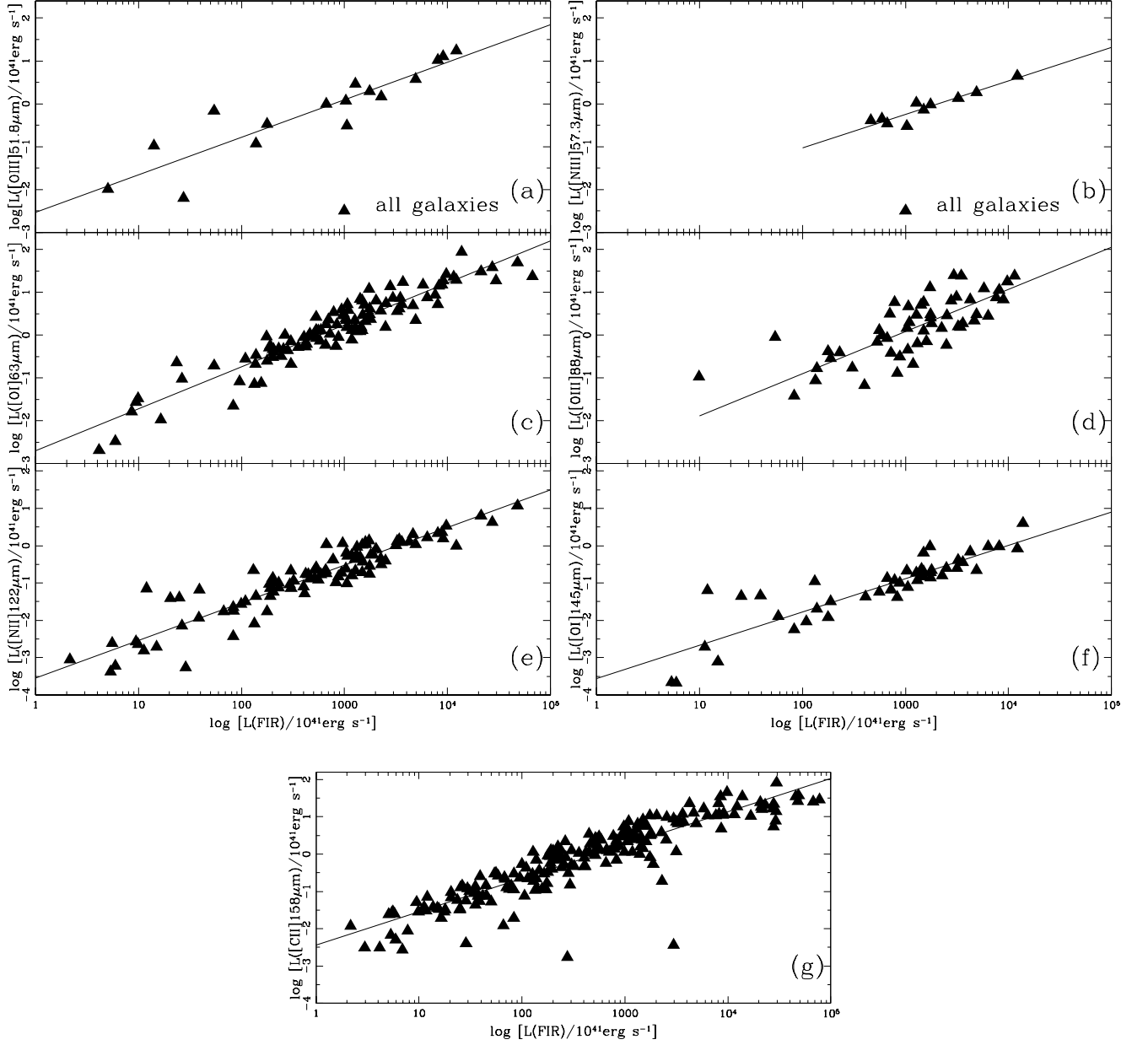
Fig. 6.— Correlations between the [OIII]52μm, [NIII]57μm, [OI]63μm, [OIII]88μm, [NII]122μm, [OI]145μm and [CII]158μm luminosity and the far-IR luminosity for the galaxies observed with the ISO-LWS spectrometer (Brauher et al. 2008).

For all correlations the hypothesis that the variables are unrelated can be rejected at a level of significance which is always less that 10^{-3}. Wu et al. (2010) presented the relation between the total infrared luminosity and the PAH emission band at 11.25μm for AGN and starburst galaxies of the 24μm flux limited intermediate redshift ($< z > \sim 0.14$) sample of 5MUSES (Helou et al. 2011, in preparation). Their result is comparable to ours. By inverting our relations we derive a slope of 1.05±011 for the Seyfert galaxies and 0.85±0.08 for the starburst galaxies, compared to their slopes of 1.00±0.04 and 0.98±0.03, respectively.

3. RESULTS

3.1. *Number counts per spectral line*

To compare and visualize our results for the three galaxy-evolution models, we need to adopt a line-detection sensitivity curve as a function of wavelength λ, an integration time, and a field of view for the simulated observations. For this purpose, we opt to use numbers relevant to future missions or facilities. For the FIR domain, we use the sensitivity curve proposed for SPICA's far infrared instrument (SAFARI), while for the submillimeter domain, we use the sensitivity curve that has
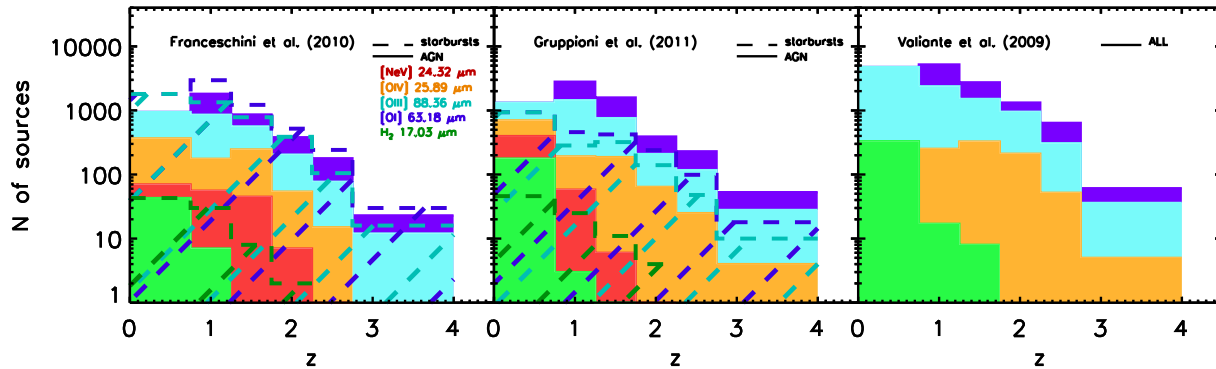
FIG. 7.— Number of objects detected per spectral line (and per object type, when applicable) in an hour-long 0.5 deg² survey with SPICA SAFARI.

been estimated for a R=1000 resolution spectrometer at the focal plane of the CCAT telescope. Details on these instruments are presented in the Appendix. Moreover, we selected a common integration time of 1 hour and a total field of view to be covered by our simulated survey of 0.5 deg². For an instrument, such as SAFARI, with a $2' \times 2'$ field of view, this corresponds to 450 hours of integration time, to be compared to 4.5 hours for a CCAT spectrometer, assuming a field of view of $20' \times 20'$.

The resulting number of AGN and starbursts that will be detectable in each line as a function of z with SAFARI is presented in Tables 1 and 2, respectively, for the Franceschini et al. (2010) model. The same results are presented in Tables 3 and 4 for the Gruppioni et al. (2011) model. The number of detectable galaxies based on the Valiante et al. (2009) model is presented in Table 5. We note that for the sake of completeness, and to assist further planning and designing of new instrumentation, we also present in Tables 1-5 the predicted number of sources that are detectable in the low−Z bins for the short-wavelength lines and those in the high-Z bins for the long-wavelength lines, even lines outside the nominal SAFARI spectral range. We have simply assumed a flat extrapolation of the SAFARI sensitivities to shorter and longer wavelengths. Tables 6, 7, and 8 present the simulation results for CCAT.

A basic result of this analysis is that the total number of detectable objects agrees to within a factor of 2−3 for most lines and z ranges, and that at least a thousand galaxies will be simultaneously detected in four lines at 5σ over a half square degree. A comparison of the output of the three models is plotted in Fig. 7 for SAFARI. A survey of the assumed sensitivity will detect bright lines (e.g., [O I] and [O III]) and PAH features in thousands of galaxies at $z>1$. Hundreds of $z>1$ AGN will be detected in the [O IV] line, and several tens of $z>1$ sources will be detected in [Ne V] and H₂. For H₂ in particular, this number corresponds to a lower limit. Our models do not account for an increase of the H₂ emission efficiency as a cooling mechanism, or for the H₂ mass content to increase with increasing z and decreasing metallicity. Neither do the applied continuum-to-line luminosity relations include sources of extremely high $L(\mathrm{H_2})/L_{\mathrm{IR}}$ ratios, associated with shock fronts due to galaxy collisions or AGN feedback mechanisms (Cluver et al. 2010; Ogle et al. 2010).

Our line detectability results are sensible when compared with predictions from local galaxy templates. To make this comparison, we used four objects with well-determined MIR and FIR spectra. These are NGC1068, a prototypical Seyfert 2 AGN, NGC4151, a well-studied type 1 AGN, the prototypical moderate-luminosity starburst M82, and a starburst-dominated ULIRG, IRAS17208-0014. Their line intensities are taken from Alexander et al. (2000); Spinoglio et al. (2005), Sturm et al. (1999); Spinoglio et al. (1997), Farrah et al. (2007); Brauher et al. (2008) and Forster Schreiber et al. (2001); Colbert et al. (1999), respectively for the four templates. We scaled the bolometric IR luminosity of all systems to 10^{12} $L_\odot$, and show which lines can be observed as a function of z in Figs. 8 and 9. This basic comparison confirms that faint lines can be detected in $z\sim1$ ULIRGs with SAFARI. Emission from [O IV] will be observable in z∼3 ULIRGs with SAFARI, while CCAT will observe [C II] out to z∼5.

In Fig. 10, and 11 we further investigate in what type of IR-bright galaxies can each line be detected as a function of z. We only make this comparison for the Franceschini et al. (2010) model, as the three models do not differ in terms of their IR-luminosity classification, and as the total number of sources is comparable in all cases. We find that for the brightest lines, such as [Si II], SAFARI will be able to observe LIRGS even at $z>3$. However, for the typical [Ne II] and [O III] $52\,\mu$m line luminosities, the transition from LIRGs to ULIRGs will occur at $z\sim2$, and for the [Ne V] and H₂ S1 lines at $z\sim1$. CCAT will be highly complementary to SPICA, as it will be able to observe the [O III] $88\,\mu$m line at $z>1.3$, where this line leaves the spectral range of SAFARI. We also find that CCAT will be a most efficient instrument for studies of [C II], an important coolant of the interstellar medium, at all $z<5$. At $3<z<4$ alone, it will detect more than 300 galaxies at 5σ level in a 0.5 deg² survey.

3.2. Line luminosity function predictions in the IR/submm

We present in Fig. 12 and 13 the predicted luminosity functions of AGN and starburst galaxies for each line and feature in the Franceschini et al. (2010) model. It is clear from the figure that the AGN line luminosity functions (dashed lines in the figure) for the lowest redshift range (0.<z<0.75) are in agreement with the local lumi-
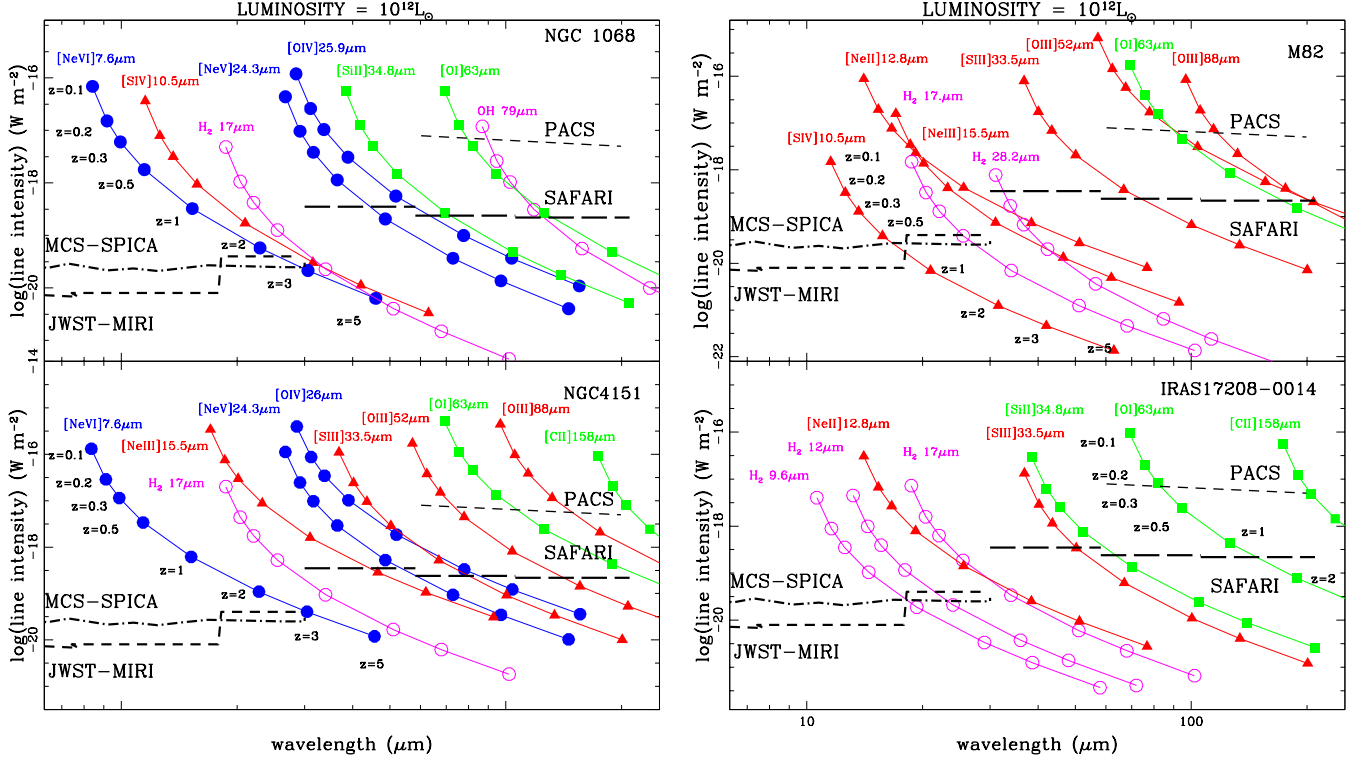
FIG. 8.— **a)**Predictions of lines observable with SPICA/SAFARI, based on local templates, scaled to an intrinsic luminosity of $10^{12} L_\odot$. Selected diagnostic lines are shown as a function of z for a type 1 AGN (NGC4151) and a type 2 AGN (NGC1068). For comparison, we overplot the 5σ (in 1 hour) sensitivity threshold of SPICA-SAFARI as a function of wavelength (see Appendix). For completeness, we also report the sensitivities for *Herschel* PACS (Poglitsch et al. 2010), for the Mid-Infrared Instrument (MIRI, Wright et al. 2004), which will be onboard the James Webb Space Telescope (Gardner et al. 2006) and which will operate from 5 to 28μm, and for the Mid-ir Camera and Spectrograph (MCS) planned for SPICA (Wada & Hirokazu 2010). **b)** Same as panel a) for a moderate-luminosity prototypical starburst (M82), and a starburst-dominated ULIRG (IRAS17208-0014).
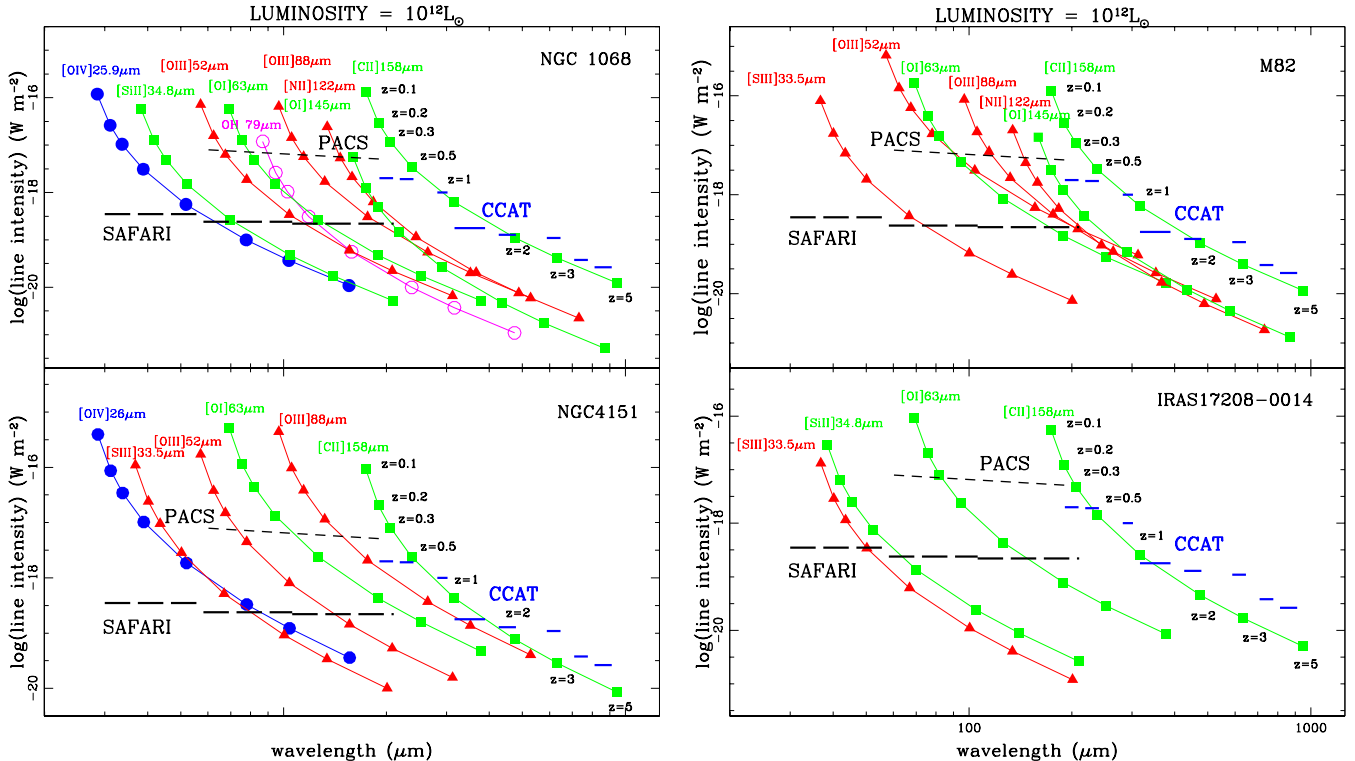

FIG. 9.— Same as Fig. 8, for long-wavelength lines, where the complementarity between SPICA and CCAT is clearly shown. For the adopted sensitivities of CCAT we refer to the Appendix.
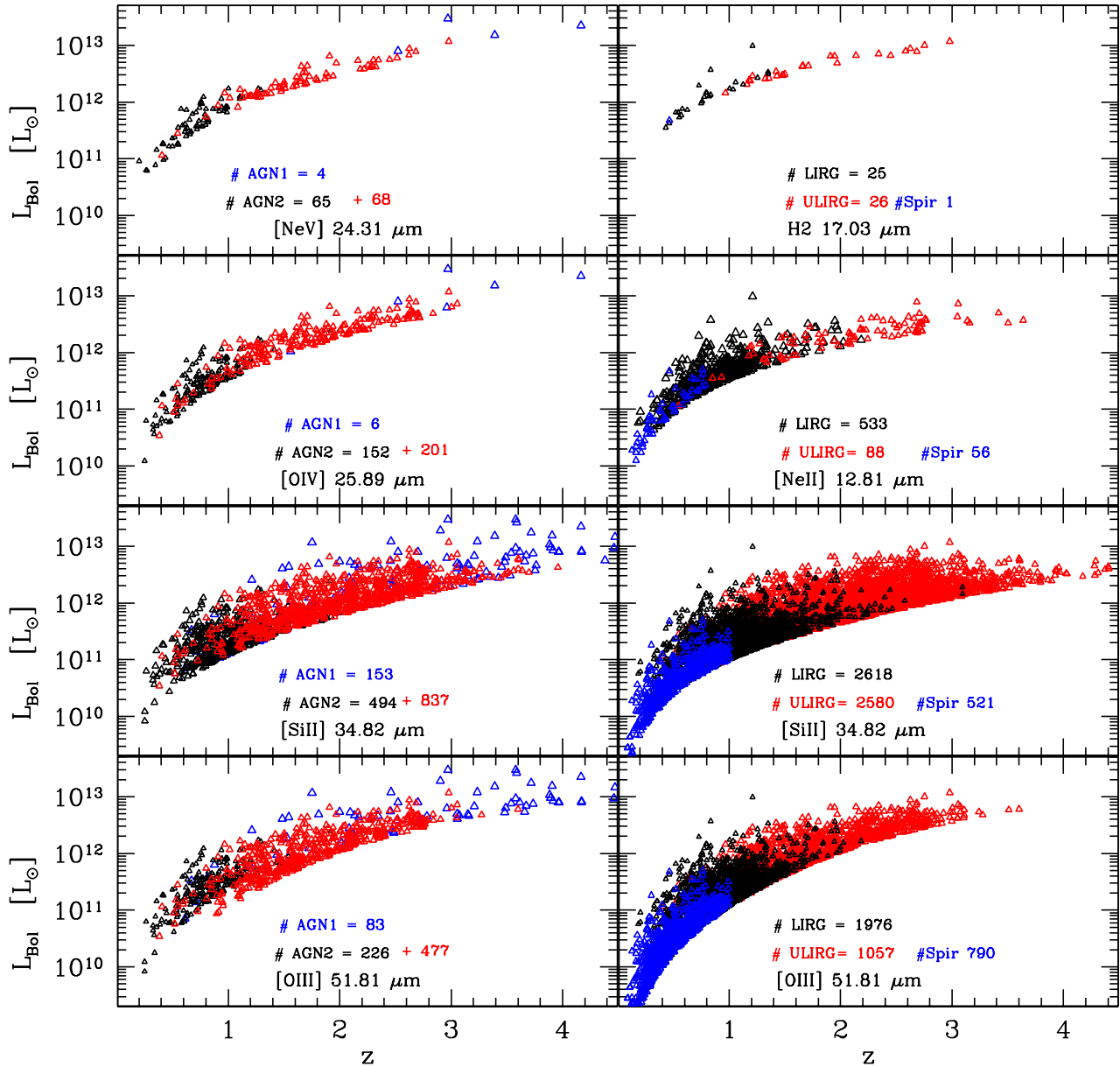
Fig. 10.— Prediction of the number of sources of a 0.5 deg^2 spectroscopic survey with SAFARI based on Franceschini et al. (2010), giving the number of detectable starburst galaxies (divided by L_{IR}) and AGN (divided by obscuration) at the 3σ level. The adopted line flux sensitivities as a function of wavelength are given in the Appendix. The left panels correspond to the AGN predictions, the right panels to the starburst predictions. As for the former, the number of type 2 AGNs associated with the LIRG and the ULIRG populations are shown separately (in black and red, respectively).

nosity functions, at an average $< z >$ of 0.03. The space densities of starburst galaxies are expected to be higher than those of AGN, for any line, except for the [OIV] line, which–as is well known–is much fainter in starburst galaxies. The volume densities of AGN drop faster with z than those of starbursts when traced by the [Ne II] and [Ne III] lines, possibly due to a saturation of the lines in AGN of high luminosities. The total number of AGN detected in the same lines is one to two orders of mag-

nitude lower than that detected for starbursts at any z. The number of sources detected in [O III] 88 μm is comparable for AGN and starbursts at all z. This result most likely differs from that for [Ne III] which comes from an ion of comparable ionization potential to O III, because of the single relationship used to convert the line luminosity to L_{IR} for long wavelength lines. This is even true for the [O I] 63 μm line, which also has a high critical density for collisional de-excitation, $\sim 10^6$ cm^{-3}, mak-
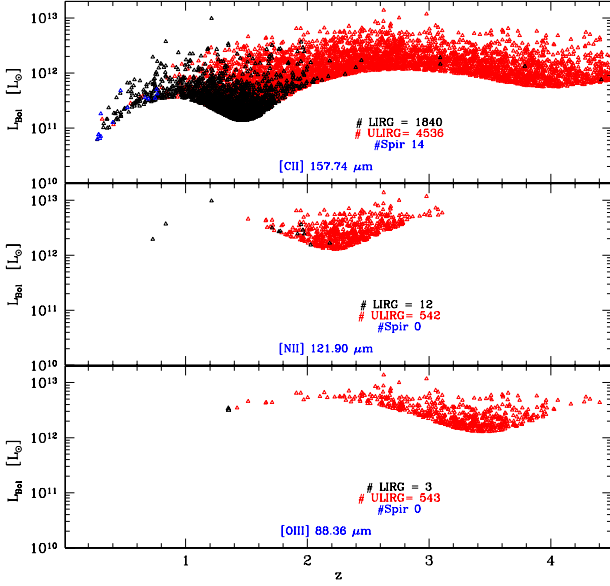
FIG. 11.— Prediction of the number of sources of a 0.5 deg² spectroscopic survey based on Franceschini et al. (2010), giving the number of detectable galaxies at the 3σ level with CCAT. The adopted line flux sensitivities as a function of wavelength are reported in the Appendix.

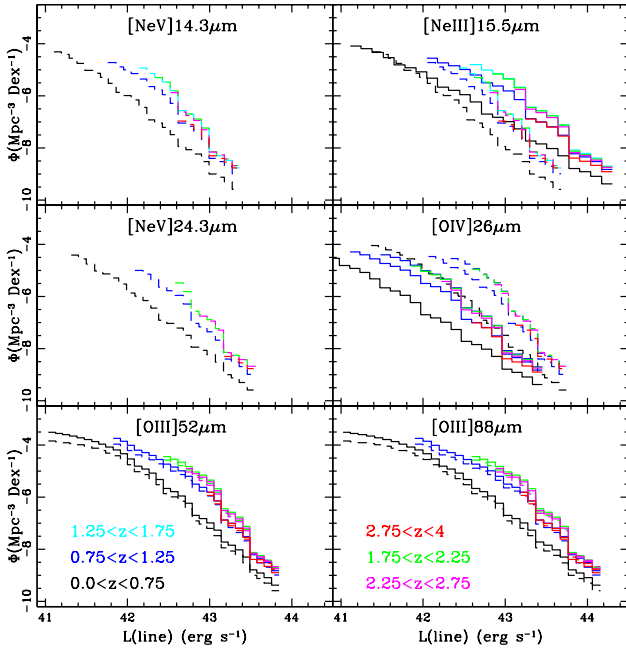FIG. 13.— Predicted line luminosity functions of PAH 11.25μm, [NeII]12.8μm, H₂ 17μm, [SiII]34.8μm , [NIII]57μm and [OI]63μm, for SAFARI. Dashed lines correspond to the predictions for AGN, while solid lines correspond to the predictions for starbursts. Where available, the comparison with the observed local LF of AGNs from Tommasin et al. (2010) is given.

creases up to $1 \lesssim z \lesssim 3$ before it drops back down at $z=4$. The same applies for tracers of star-formation, reproducing the suggested coevolution of black hole growth and stellar mass build-up.

4. DISCUSSION: NEW PARAMETER-SPACE COVERAGE BY SPICA AND CCAT

Which of the questions raised in the Introduction will the proposed future telescopes address? The lines predominantly emitted by ions in star-forming complexes, like [Si II], [C II], and [Ne II], will be detected in $L_{IR} > 10^{11} L_{\odot}$ systems at least out to $z \sim 2$. They will also be detected in $10^{10} L_{\odot} < L_{IR} < 10^{11} L_{\odot}$ galaxies at least out to $z \sim 1$. This result indicates that star-formation tracers will be detected and compared for the sources that are mainly responsible for the formation of present-day ellipticals. The creation of line-ratio diagnostic diagrams, and the comparison of the line to IR continuum luminosities in hundreds of sources will help us, in combination with imaging data, to further address the star-formation bimodality, and to obtain a more coherent picture of the intermediate/high-z IR-bright populations. Several sources will be detected with CCAT even past the peak of star-formation activity at $z > 3$ in the strong [C II] line, which will help us constrain the shape of Lilly-Madau diagrams at such high redshifts.

To date, the detection of FIR fine-structure lines has only been achieved in lensed $z > 1$ systems. *Herschel* PACS detected the [O III] 52μm line with a flux of $9 \times 10^{-19} \text{Wm}^{-2}$ in IRAS F10214+4724 at $z=2.28$ (Sturm et al. 2010). In a $z=1.32$ source, MIPS J142824.0+352619, [O III] 52μm and [O I] 63μm were detected with fluxes of 3.7 and $7.8 \times 10^{-18} \text{Wm}^{-2}$, respectively (Sturm et al.

FIG. 12.— Predicted line luminosity functions of [NeV]14.3μm, [NeIII]15.5μm, [NeV]24.3μm, [OIV]26μm, [OIII]52μm and [OIII]88μm, for SAFARI. Dashed lines correspond to the predictions for AGN, while solid lines correspond to the predictions for starbursts. Where available, the comparison with the observed local LF of AGNs from Tommasin et al. (2010) is given.

ing it bright in AGN. The contamination of the [O IV] AGN luminosity functions from starbursts is minimal all the way through $z=4$. The volume density of actively accreting black holes as traced by [O IV] and [Ne V] in-

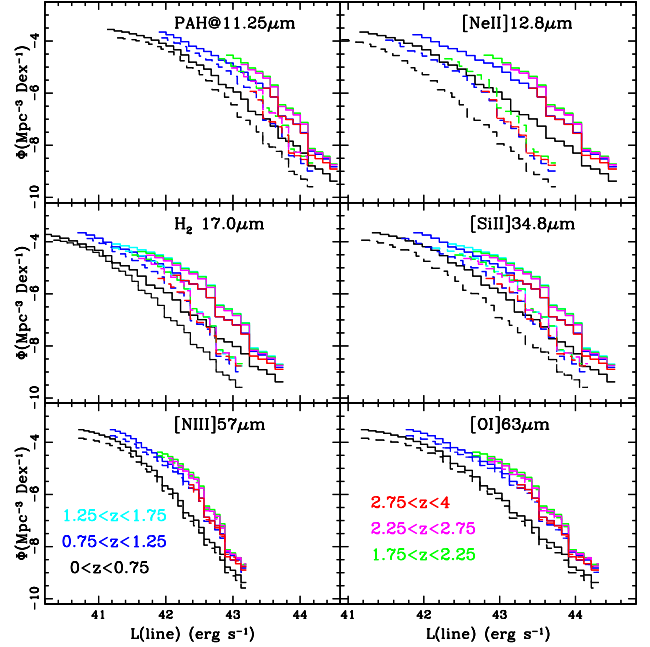2010). The [O III] 88μm line was detected at the Caltech Submillimeter Observatory (CSO) with the ZEUS spectrometer (Ferkinhoff et al. 2010b) in APM 08279+5255 at z=3.9 and SMM J02399-0136 at z=2.8 (Ferkinhoff et al. 2010a), with fluxes of 2.68 and 6.04 $\times10^{-18}$Wm^{-2}. All four systems are lensed galaxies, with magnification factors estimated to be in the range $2.4-90$ (Egami et al. 2000; Ao et al. 2008; Riechers et al. 2009; Ivison et al. 2010). Such experiments were not possible for unlensed galaxies with the present-day missions, leaving ample room for new discoveries for SPICA and CCAT.

The recent detection of [NII]122μm (Ferkinhoff et al. 2011) and [CII]158μm (Stacey et al. 2010) lines in a few high redshift galaxies with the ZEUS spectrometer (Ferkinhoff et al. 2010b) at the CSO shows that these lines can be much brighter than in local galaxies. The [NII]122μm line to FIR luminosity ratio is 2-10 times higher in the two observed galaxies (H1413+117 and SMMJ02399-0136) than in the local galaxies that we used for deriving the line to continuum relations adopted for our predictions. Similarly the [CII]/FIR luminosity ratio in the $1 < z < 2$ galaxies can be twice as high as the value observed in the local Universe, despite having a large rage from 0.024% to 0.65% . This indicates that our estimates can be considered conservative, and that CCAT could observe many more galaxies than what shown in our predictions. It could potentially trace the star formation history of galaxies back to very high redshift.

A simple conversion of the SAFARI sensitivity limit into an H_2 line flux and mass indicates that detection of H_2-bright galaxies at z>6 will be feasible over large areas. An S1 flux of 2.5×10^{-19} W m^{-2} at a typical temperature of 300K, yields an H_2 mass of $3\times10^{10}\,M_\odot$ at z=6. Cosmological simulations indicate that $z\sim6$ galaxies of such a molecular gas mass can exist (Obreschkow & Rawlings 2009). Unless there is a significant increase in the efficiency of H_2 to cool the ISM, or unless there is a considerable number of sources with an AGN jet-ISM interaction that leads to very high L(H_2)/L_{IR} ratios (Ogle et al. 2010), our conclusion will not hold at $z\sim10$. At that z, the same temperature and S1 flux correspond to a mass of $10^{11}\,M_\odot$. Even though the H_2 (0-0)S0 line at $28.03\,\mu$m will be in the spectral range of CCAT at $z> 6$, its detection will be equally hard: assuming an S0 flux of 2×10^{-19} W m^{-2} and an ortho-to-para ratio of 3, the minimum detectable H_2 mass would be $\sim10^{11}\,M_\odot$ at z=6. SPICA will thus be unique for H_2 studies seeking the end of the reionization era.

Another parameter space unique to SPICA will be the detection of resolved [O IV] $25.89\,\mu$m emission up to $z\sim4$. The calibration of the widths of high-ionization MIR lines, as probes of the narrow-line-region kinematics, to the black hole mass was attempted with *Spitzer* for sources out to z=0.3 (Dasyra et al. 2008, 2011). It might be useful for the mid-infrared instrument of JWST, which will be able to observe the [Ne V] $14.32\,\mu$m line out to $z\sim0.8$. The breakthrough for such studies will come however from SPICA. SAFARI will access the z>1 Universe and go past its accretion-rate-history peak. The shape of the accretion rate functions will be then compared to the shape of the mass functions of the obscured and unobscured black holes upon which the material is accreted. The inclusion of obscured black holes in mass

functions of unobscured AGN (e.g., Vestergaard & Osmer 2009) could change their observed volume-density normalization factors and shapes. The most obscured AGN are thought to be missing from a redshift of only 1 (e.g., Gilli et al. 2007), unlike the bulk of the black hole growth that is thought to be occurred at $z > 1$.

5. SUMMARY

We used three galaxy formation and evolution models, constrained by luminosity functions from multi-wavelength observations, to predict the number of star-forming and active galaxies that are observable in any IR luminosity bin with look-back time. We converted the number counts of galaxies per IR luminosity to number counts of galaxies per line luminosity using several (new) line-to-continuum conversion relations, built upon local AGN and starburst galaxy samples. We compute our results for an hour-long integration/FoV half-square-degree survey, and for the sensitivity values of SPICA SAFARI and CCAT. Their anticipated values are 2.5×10^{-19} W m^{-2} at $160\,\mu$m and 1.1×10^{-19} W m^{-2} at $620\,\mu$m, respectively. These telescopes/instruments were selected because they are designed to be survey machines, able to perform large blind cosmological surveys in reasonable integration times. We find that SAFARI will detect thousands of z>1 galaxies in bright low-ionization fine-structure lines such as [Si II] and [Ne II], and several tens of $1 < z < 2$ galaxies in fainter lines such as [O IV], [Ne V] and H_2 (0-0)S1. For the bright lines, normal galaxies will be observed out to $z\sim1$, LIRGs out to $z\sim2$, and ULIRGs to even higher z. This means that studies of the ionized gas properties in the galaxies that form the present day massive ellipticals will be feasible. AGN/star-formation diagnostic diagrams will be obtained for different classes of IR-bright galaxies at $1 < z < 2$, which will enable us to not only look for a redshift evolution of line ratios, but also for a luminosity evolution within each z range. Further tests of the black hole growth - galaxy build-up coevolution scenario will be performed, as the creation of accretion-rate functions and mass functions will be determined out to $z\sim4$, for both obscured and unobscured black holes using the [O IV] line. Over large areas, SAFARI could also be able to detect H_2 at $z\gtrsim6$, and help constrain the end of the reionization era. In the light of the current findings at ground-based submillimeter telescopes of substantially brighter fine structure lines in high redshift galaxies compared to local galaxies, we are even more confident that CCAT will be unique for studying the star formation history of galaxies back to very high redshift.

APPENDIX

DESCRIPTION OF THE SPICA MISSION AND THE CCAT FACILITY TO BE USED FOR FUTURE, BLIND COSMOLOGICAL SURVEYS IN THE IR AND SUBMM

The deep cosmological surveys undertaken by ISO (Kessler et al. 1996), *Spitzer* (Werner et al. 2004), AKARI (Murakami et al. 2007; Goto et al. 2010), WISE (Wright et al. 2010), and *Herschel* (Pilbratt et al. 2010) will have produced catalogues containing the fluxes of many tens of thousands of IR-bright sources by the early 2020's. These catalogues will provide excellent targets to be followed up by ALMA (Brown, Wild & Cunningham 2004; Wootten 2008), JWST (Gardner et al. 2006), SPICA (Swinyard et al. 2009), and CCAT (Sebring 2010). Among the listed facilities, JWST and ALMA will be more suited to deep follow-up spectroscopy of known targets. SPICA and CCAT will be suited for performing blind large-scale spectro-photometric surveys, because of the wide field of view (of several arcminutes squared) of their instruments. Covering different wavelength ranges, these two instruments will be highly complementary. In the rest of the Appendix, we provide details of their present-day design concepts.

SPICA is a proposed JAXA-led astronomical mission with suggested contributions by European, Korean, and possibly US institutions, and with a launch date planned in the early 2020s (Swinyard et al. 2009). With a 3-m mirror that is actively cooled to <6K, and a state-of-the art focal plane instrument suite, SPICA will make imaging and spectroscopic observations over the 5-210μm spectral range with unprecedented sensitivity. It will offer an improvement in raw photometric sensitivity with respect to *Herschel* of two orders of magnitude in the FIR. In the MIR, it will extend the capabilities of JWST with an uninterrupted spectral coverage in the range 5-38μm. The Mid Infrared Camera and Spectrometer (MCS) planned for SPICA (Wada & Hirokazu 2010; SPICA Study Team Collaboration 2010) is an integral field unit with a field of view of $12'' \times 6''$ at 10-20μm and $12'' \times 12.5''$ at 19.5-36.1μm. Its $5\,\sigma$, 1 hour sensitivity is in the range 2-2.5 $\times 10^{-20}Wm^{-2}$ (Wada & Hirokazu 2010). Observing capability in the FIR is provided for SPICA by SAFARI (Swinyard et al. 2009; SPICA Study Team Collaboration 2010). Proposed by a consortium of European institutes (with Canadian and Japanese participation), SAFARI is an imaging Fourier Transform Spectrometer (FTS) with a field of view of $2' \times 2'$. The FTS provides an instantaneous spectral coverage of the 34 - 210μm wavelength range and spectral resolution modes with $\lambda/\Delta\lambda$ of 2000 (at 100 μm), $\sim$ few hundred, or even as low as $20 < \lambda/\Delta\lambda < 50$. With its sensitive superconducting transition edge sensor (TES) detectors (Khosropanah et al. 2010), SAFARI will offer a factor of $\sim$100 increase in raw sensitivity in the continuum, and $\sim$15 in high-resolution mode spectroscopy compared to *Herschel* PACS (Poglitsch et al. 2010). The improvement in spectral mapping speed over PACS will be of more than 100 at $\lambda/\Delta\lambda\sim$ 2000. Assuming a Noise Equivalent Power (NEP) of $2 \times 10^{-19}W/\sqrt{Hz}$ for the SAFARI detectors, the $5\,\sigma$, 1 hour detection limits are predicted to be 4.16, 2.58, 1.89 and 2.48 $\times 10^{-19}$Wm^{-2} for the four planned spectral bands centred at 48, 85, 135 and 160μm, respectively, for an unresolved line at $\lambda/\Delta\lambda\sim$ 2000 (Swinyard, B., 2011, priv. comm.).

The Cerro Chajnantor Atacama Telescope (CCAT) will be a 25m submm wave telescope to be constructed near the summit of Cerro Chajnantor (Sebring 2010). The CCAT science case, observatory requirements, and conceptual design were developed as part of a study jointly funded by Cornell and Caltech/JPL, which resulted in a Feasibility/Concept Design Study Report, available at: *http://www.submm.org/doc/2006-01-ccat-feasibility.pdf*. The design of the CCAT telescope is currently undergoing changes to increase the field of view from 20×20 arcminutes square to 1 square degree (Sebring 2010). This would substantially increase the survey capability of the telescope. CCAT will carry out spectroscopic surveys of submm galaxies, using multi-object versions of broadband direct-detection grating spectrometers such as Z-Spec (Bradford et al. 2004) and ZEUS (Ferkinhoff et al. 2010b), now in use at the CSO. Conceptual development indicates that spectrometers capable of observing 10-100 objects simultaneously while spanning multiple atmospheric windows will be feasible (Stacey et al. 2006) . Sensitivity estimates based on the 25 m telescope CCAT telescope with a 10 μm rms surface on Cerro Chajnantor (5600 m elevation) for a spectrometer with a resolution of 1000 (5σ, 1 hour) that include wavelength-dependent, typical precipitable water vapor corrections are: 2.0, 1.9 and 1.0 $\times 10^{-18}$Wm^{-2} at 200μm, 230μm and 291μm respectively, 1.8, 1.3 and 1.1 $\times 10^{-19}$Wm^{-2} at 350μm, 450μm and 620μm respectively and 3.8 and 2.6 $\times 10^{-20}$Wm^{-2} at 740μm and 865μm respectively (Stacey, G. 2011, private comm.).

REFERENCES

Alexander, T. et al. 2000, ApJ, 536, 710
Altieri, B., et al. 2010, A&A, 518, L17
Ao, Y., Weiß, A., Downes, D., Walter, F., Henkel, C., Menten, K. M. 2008, A&A, 491, 747
Austermann, J.E., et al. 2010, MNRAS, 401, 160
Barger, A.J., et al. 1998, Nature, 394, 248
Barmby, P. et al. 2006, ApJ, 642, 126
Bernard-Salas, J., Spoon, H. W. W.; Charmandaris, V. et al. 2009, ApJS, 184, 230
Berta, S., et al. 2010, A&A, 518, L30

Borys, C., Chapman, S., Halpern, M., Scott, D. 2003, MNRAS, 344, 385
Brown, R.L., Wild, W. & Cunningham, C. 2004, AdSpR, 34, 555
Bradford, C.M., et al. 2004, SPIE, 5498, 257
Brauher, J.R., Dale, D.A., Helou, G. 2008, ApJS, 178, 280
Caputi, K. I., Dunlop, J. S., McLure, R. J., Roche, N. D., 2005, MNRAS, 361, 607
Clegg, P.E. et al 1996, A&A, 315, L38
Clements, D.L., et al. 2010, A&A, 518, L8
Cluver, M. E., et al. 2010, ApJ, 710, 248
Colbert, J. et al. 1999, ApJ, 511, 721

Coppin, K. et al. 2006, MNRAS, 372, 1621
Cowie, L.L. et al. 1996, AJ, 112, 839
Daddi, E., et al. 2005, ApJ, 631, L13
Daddi, E. et al. 2010, ApJ, 714, L118
Dale, D.A. et al. 2006, ApJ, 646, 161
Dasyra, K. M., et al. 2006, ApJ, 638, 745
Dasyra, K. M., et al. 2008, ApJ, 674, L9
Dasyra, K. M., et al. 2009, ApJ, 701, 1123
Dasyra, K. M., Ho, L. C., Netzer, H., Combes, F., Trakhtenbrot, B., Sturm, E., Armus, L., & Elbaz, D., ApJ, in press, arXiv:1107.3397
Eales, S., et al. 2010, PASP, 122, 499
Egami, E., Neugebauer, G., Soifer, B. T., Matthews, K., Ressler, M., Becklin, E. E., Murphy, T. W., Jr., Dale, D. A. 2000, ApJ, 535, 561
Elbaz D. et al. 1999 A&A, 351, L37
Fabian, A.C. 1999, MNRAS, 308, L39
Fadda, D. et al. 2004, AJ....128....1
Farrah, D. et al.. 2007, ApJ, 667, 149
Ferkinhoff, C., Hailey-Dunsheath, S., Nikola, T., Parshley, S.C., Stacey, G.J., Benford, D.J., Staguhn, J.G. 2010a, ApJL, 714, L147
Ferkinhoff, C., Nikola, T., Parshley, S.C., Stacey, G.J., Irwin, K.D., Cho, H-M., & Halpern, M. 2010b, SPIE, 7741, E26F
Ferkinhoff, C., et al. 2011, ApJ, 740, L29
Ferrarese, L. & Merrit, D. 2000, ApJ, 539, L9
Ferrarese, L. & Ford, H., 2005, Space Science Rev., 116, 523
Forster Schreiber, N.M., Genzel, R., Lutz, D., Kunze, D., Sternberg, A. 2001, ApJ, 552, 544
Franceschini, A., Rodighiero, G., Vaccari, M., Berta, S., Marchetti, L., Mainetti, G. 2010, A&A, 517, 74F
Gardner, J.P. et al 2006, SSRv, 123, 485
Genzel, R., et al. 1998, ApJ, 498, 579
Genzel, R. et al 2010, MNRAS, 407, 2091
Gilli, R., Comastri, A., & Hasinger, G. 2007, A&A, 463, 79
Glenn, J. et al. 2010, MNRAS, 409, 109
Goto, T., et al. 2010, A&A, 514A, 6
Gracia-Carpio J. et al. 2011, ApJ, 728, L7
Greve, T.R., et al. 2004, MNRAS, 354, 779
Gruppioni C. et al. 2002, MNRAS, 335, 831
Gruppioni, C. et al. 2008, ApJ, 684, 136
Gruppioni, C. et al. 2010, A&A, 518, L27
Gruppioni, C., Pozzi, F., Zamorani, G., Vignali, C. 2011, MNRAS, in press, and arXiv:1105.1955
Gultekin, K., et al. 2009, ApJ, 698, 198
Houck, J.R. et al. 2004, ApJS, 154, 18
Houck, J.R., et al. 2005, ApJ, 622, 105
Huang, J.-S., et al. 2009, ApJ, 700, 183
Hughes, D.H. et al. 1998, Nature, 394, 24
Kessler, M.F. et al. 1996, A&A, 315, L27
Khosropanah, P. et al 2010, Proc. SPIE, 7731, E14
Kormendy, J. & Richstone, D. 1992, ApJ, 393, 559
Ivison, R. J., Smail, I., Papadopoulos, P.P., Wold, I., Richard, J., Swinbank, A.M., Kneib, J.-P., Owen, F.N. 2010, MNRAS, 404, 198
Lacy, M. et al. 2004, ApJS, 154, 166
Laurent, G.T., et al. 2005, ApJ, 623, 742
Le Floc'h, E., et al. 2004, ApJS, 154, 170
Lu, Y., et al. 2010, MNRAS, 404, 176
Ly, C., Malkan, M., Hayashi, M., Motohara, K., Kashikawa, N., Shimasaku, K., Nagao, T., Grady, C. 2011, ApJ, 735, 91
Magorrian, J. et al. 1998, AJ, 115, 2285
Marconi, A., Risaliti, G., Gilli, R., Hunt, L.K., Maiolino, R., Salvati, M. 2004, MNRAS, 351, 169
Merloni, A., Rudnick, G., Di Matteo, T. 2004, MNRAS, 354, L37
Metcalfe L. et al. 2003, A&A, 407, 791
Mor, R., Netzer, H., Elitzur, M. 2009, ApJ, 705, 298
Mullaney, J.R. et al. 2010, MNRAS, 401, 995
Murakami, H. et al. 2007, PASJ, 59, 369
Nguyen, H. T., Schulz, B., Levenson, L., et al. 2010, A&A, 518, L5
Obreschkow, D. & Rawlings, S. 2009, ApJ, 696, L129

Oliver, S., et al. 2010, A&A, 518, L210
Ogle, P., Boulanger, F., Guillard, P., Evans, D. A., Antonucci, R., Appleton, P. N., Nesvadba, N., & Leipski, C. 2010, ApJ, 724, 1193
Papovich, C. et al. 2004, ApJS, 154, 70
Papovich, C. et al. 2006, AJ, 132, 231
Perera, T.A. et al. 2008, MNRAS, 391, 1227
Perez-Gonzalez, P.G. et al. 2005, ApJ, 630, 82
Pilbratt, G.L. et al. 2010, A&A, 518, L1
Poglitsch, A. et al. 2010, A&A, 518, L2
Powell, L.C., et al., 2011arXiv1102.4195P
Reddy N.A., et al. 2010, ApJ, 712, 1070
Richstone, D. et al. 1998, Nature, 395, 14
Riechers, D.A., Walter, F., Carilli, C.L., Lewis, G.F. 2009, ApJ, 690, 463
Rigby, J.R., et al. 2004, ApJS, 154, 160
Rodighiero G. et al., 2004, A&A, 427, 773
Rodighiero, G., Vaccari, M., Franceschini, A., et al., 2010, A&A, 515, A8
Rush, B., Malkan, M.A. & Spinoglio, L. 1993, ApJS, 89, 1
Sanders, D.B. & Mirabel, I.F. 1996, ARA&A, 34, 749
Scott, S.E., et al 2002, MNRAS, 331, 817
Scott, K.S., et al. 2008, MNRAS, 385, 2225
Sebring, T., 2010, SPIE, 7733, 59
Shankar, F., Bernardi, M., Haiman, Z. 2009, ApJ, 694, 867
Shim, H., Colbert, J., Teplitz, H., Henry, A., Malkan, M., McCarthy, P., Yan, L. 2009, ApJ, 696, 785
Shupe D. L. et al. 2008, AJ, 135, 1050
Smail, I., Ivison, R. J., Blain, A. W. 1997, ApJ, 490, L5
Smith, J.D.T. et al. 2007, ApJ, 656, 770
SPICA Study Team Collaboration, 2010. SPICA Assessment Study Report for ESA Cosmic Vision 2015-2025 Plan, ESA/SRE(2009) 6 December 2009, arXiv1001.0709S.
Spinoglio, L. & Malkan, M.A. 1992, ApJ, 399, 504
Spinoglio, L., et al. 1997, Extragalactic Astronomy in the Infrared. Edited by G. A. Mamon, Trinh Xuan Thuan, and J. Tran Thanh Van. Paris: Editions Frontieres, p.333
Spinoglio, L., Malkan, M., Rush, B., Carrasco, L., Recillas-Cruz, E. 1995, ApJ, 453, 616
Spinoglio, L., Andreani, P., Malkan, M., 2002, ApJ, 572, 105
Spinoglio, L., Malkan, M.A., Smith, H.A., González-Alfonso, E., Fischer, J. 2005, ApJ, 623, 123
Stacey, G. J. et al 2006, SPIE, 6275, 47
Stacey, G. J. et al 2010, ApJ, 724, 957
Stern, D. et al. 2005, ApJ, 631, 163
Sturm, E. et al. 1999, ApJ, 512, 197
Sturm, E. et al. 2010, A&A, 518, L36
Schweitzer, M. et al. 2006, ApJ, 649, 79
Swinyard, B., Nakagawa, T. et al. 2009, Experimental Astronomy, 23, 193
Tremaine, S. et al. 2002, ApJ, 574, 740
Tommasin, S., Spinoglio, L., Malkan, M.A., Smith, H., Gonzlez-Alfonso, E., Charmandaris, V. 2008, ApJ, 676, 836.
Tommasin, S., Spinoglio, L., Malkan, M., Fazio, G., 2010, ApJ, 709, 1257
Treu, T., Malkan, M., Blandford, R., 2004, ApJ, 615, 97
Valiante, E., Lutz, D., Sturm, E., Genzel, R., Chapin, E.L. 2009, ApJ, 701, 1814
Vaccari, M., et al. 2010, A&A, 518, L20
Vestergaard, M., & Osmer, Patrick S, 2009, ApJ, 699, 800
Wada, T. & Hirokazu, K. 2010, Proc. SPIE, 7731, E23
Webb, T.M., et al. 2003, ApJ, 582, 6
Werner, M.W. et al. 2004, ApJS, 154, 1
Wise, J. H., & Abel, T. 2007, ApJ, 671, 1559
Wootten, A. 2008, Ap&SS, 313, 9
Wright, E.L. et al 2010, AJ, 140, 1868
Wright, G.S. et al. 2004, Proc. SPIE 5487, 653
Wu, Y. et al. 2010, ApJ, 723, 895

TABLE 1
Number of AGN detectable in a SAFARI survey of 0.5^2 in IR lines as a function of redshift at 5σ (3σ) in 1 hr. integration per FoV, following Franceschini et al. (2010)

line/redshift	0<z<0.75	0.75<z<1.25	1.25<z<1.75	1.75<z<2.25	2.25<z<2.75	2.75<z<4	all redshifts #
PAH(11.25μm)	687. (945.) †	633. (1449.) †	439. (703) †	54.0 (138.)	5.85 (47.7)	⋯ (1.35)	60.0 (187.) ‡
[NeII] 12.81μm	152. (366.) †	122. (247.) †	14.4 (45.0)	0.90 (6.75)	⋯ (0.45)	⋯ (⋯)	15.3 (52.2) ‡
[NeV] 14.32 μm	43.2 (152.) †	20.2 (82.3) †	0.45 (5.85)	⋯ (⋯)	⋯ (⋯)	⋯ (⋯)	0.45 (5.85) ‡
[NeIII] 15.55μm	152. (366.) †	35.1 (82.3)	5.85 (45.0)	0.45 (1.80)	⋯ (0.45)	⋯ (⋯)	41.4 (130.) ‡
H₂(17.03μm)	10.8 (43.2) †	⋯ (6.75)	⋯ (0.45)	⋯ (⋯)	⋯ (⋯)	⋯ (⋯)	⋯ (7.20) ‡
[SIII] 18.71μm	43.2 (106.) †	3.15 (11.2)	⋯ (0.90)	⋯ (⋯)	⋯ (⋯)	⋯ (⋯)	46.3 (118.)‡
[NeV] 24.32μm	26.6 (69.8)	11.2 (55.8)	14.4 (45.0)	0.90 (6.75)	⋯ (0.90)	⋯ (⋯)	53.1 (178.)
[OIV] 25.89μm	152. (366.)	82.3 (246.)	73.8 (246.)	17.1 (54.0)	0.90 (14.8)	⋯ (⋯)	326. (857.)
[SIII] 33.48μm	69.8 (210.)	122. (247.)	45.0 (174.)	6.75 (32.8)	0.90 (14.8)	⋯ (⋯)	244. (679.)
[SiII] 34.81μm	210. (366.)	333. (633.)	174. (439.)	54.0 (204.)	14.8 (121.)	1.35 (11.7)	787. (1775.)
[OIII] 51.81μm	464. (687.)	333. (633.)	246. (563.)	54.0 (204.)	14.8 (28.8)	⋯ (0.90) †	892. (2117.) ‡
[NIII] 57.32μm	106. (281.)	55.8 (176.)	14.4 (73.8)	⋯ (0.90)	⋯ (⋯)	⋯ (⋯)	176. (532.)
[OI] 63.18μm	687. (945.)	1128. (1817.)	563. (863.)	204. (381.)	47.7 (179.)	4.50 (22.5) †	2833. (4184.) ‡
[OIII] 88.35μm	687. (945.)	459. (856.)	246. (563.)	88.2 (204.) †	28.8 (77.4) †	0.90 (11.7) †	1392. (2364.) ‡

*Notes: #: total number of AGN inside detectable the SAFARI spectral range; †: outside the SAFARI spectral range;‡: excluding detections outside the SAFARI spectral range.

TABLE 2
Number of starburst galaxies detectable in a SAFARI survey of 0.5^2 in IR lines as a function of redshift at 5σ (3σ) in 1 hr. integration per FoV, following Franceschini et al. (2010)

line/redshift	0<z<0.75	0.75<z<1.25	1.25<z<1.75	1.75<z<2.25	2.25<z<2.75	2.75<z<4	all redhifts #
PAH(11.25μm)	1023. (1519.) †	974. (1790.) †	608. (984.) †	119. (277.)	39.1 (105.)	1.80 (15.7)	160. (398.) ‡
[NeII] 12.81μm	636. (1023.) †	692. (1340.) †	239. (460.)	72.9 (187.)	20.2 (64.3)	0.90 (6.30)	333. (718.) ‡
[NeIII] 15.55μm	115. (254.) †	80.5 (118.)	37.3 (101.)	9.00 (44.1)	1.35 (8.10)	0.45 (1.80)	129. (273.) ‡
H₂(17.03μm)	28.8 (43.2) †	9.90 (29.7)	2.25 (7.65)	0.45 (1.80)	⋯ (⋯)	⋯ (⋯)	12.6 (39.1)‡
[SIII] 18.71μm	176. (355.) †	50.8 (118.)	19.3 (61.6)	2.70 (22.9)	1.35 (8.10)	⋯ (0.45)	250. (566.)‡
[OIV] 25.89μm	2.70 (9.45)	1.80 (9.90)	1.35 (7.65)	0.45 (0.90)	⋯ (⋯)	⋯ (⋯)	6.30 (27.9)
[SIII] 33.48μm	355. (636.)	495. (974.)	337. (608.)	119. (277.)	64.3 (164.)	6.30 (30.1)	1377. (2689.)
[SiII] 34.81μm	482. (816.)	974. (1790.)	608. (984.)	277. (519.)	164. (339.)	30.1 (81.4)	2535. (4529.)
[OIII] 51.81μm	816. (1257.)	495. (974.)	337. (783.)	72.9 (277.)	2.25 (39.1)	⋯ (0.90) †	1723. (3330.) ‡
[NIII] 57.32μm	176. (482.)	80.5 (258.)	19.3 (101.)	⋯ (1.80)	⋯ (⋯)	⋯ (⋯)	276. (843.)
[OI] 63.18μm	1257. (1808.)	1790. (2960.)	783. (1221.)	277. (519.)	64.3 (242.)	6.30 (30.1) †	4171. (6750.) ‡
[OIII] 88.35μm	1257. (1808.)	692. (1340.)	337. (783.)	119. (388.) †	39.1 (105.) †	0.90 (15.7) †	2286. (3931.) ‡

*Notes: #: total number of AGN inside detectable the SAFARI spectral range; †: outside the SAFARI spectral range;‡: excluding detections outside the SAFARI spectral range.

TABLE 3
Number of AGN detectable in a SAFARI survey of 0.5^2 in IR lines as a function of redshift at 5σ (3σ) in 1 hr. integration per FoV, following Gruppioni et al. (2011)

line/redshift	0<z<0.75	0.75<z<1.25	1.25<z<1.75	1.75<z<2.25	2.25<z<2.75	2.75<z<4	all redhifts #
PAH(11.25μm)	1057.(1451.) †	1076. (2317.) †	486. (1126.)†	64.3 (148.)	13.9 (75.6)	0.90 (7.65)	79.1 (231.)‡
[NeII] 12.81μm	398.(701.) †	111. (326.) †	9.90 (28.8)	3.60 (12.6)	0.45 (1.80)	⋯ (⋯)	14.0 (43.2)‡
[NeV] 14.32 μm	177.(398.) †	9.90 (58.0) †	0.90 (5.85)	⋯ (0.90)	⋯ (⋯)	⋯ (⋯)	0.90 (6.75)‡
[NeIII] 15.55μm	398.(701.) †	16.6 (58.0)	5.85 (28.8)	1.80 (6.30)	0.45 (1.80)	⋯ (0.45)	24.7 (95.3)‡
H₂(17.03μm)	82.3(177.) †	0.45 (3.15)	⋯ (0.90)	⋯ (⋯)	⋯ (⋯)	⋯ (⋯)	0.45 (4.05)‡
[SIII] 18.71μm	177.(398.) †	1.80 (5.40)	0.45 (1.80)	⋯ (0.45)	⋯ (0.45)	⋯ (⋯)	2.25 (10.3)‡
[NeV] 24.32μm	124.(240.)	5.40 (32.8)	9.90 (28.8)	3.60 (12.6)	0.45 (3.60)	⋯ (⋯)	143. (318.)
[OIV] 25.89μm	491.(701.)	58.0 (192.)	47.7 (187.)	22.0 (64.3)	3.60 (25.2)	0.90 (4.05)	623. (1174.)
[SIII] 33.48μm	240.(491.)	111. (326.)	28.8 (121.)	12.6 (39.1)	6.75 (25.2)	0.90 (4.05)	400. (1006.)
[SiII] 34.81μm	491.(701.)	512. (1076.)	121. (486.)	64.3 (209.)	45.9 (170.)	7.65 (28.3)	1242. (2670.)
[OIII] 51.81μm	814.(1184.)	512. (1076.)	188. (759.)	64.3 (209.)	6.75 (45.9)	⋯ (⋯)	1585. (3274.)
[NIII] 57.32μm	398.(701.)	32.8 (192.)	9.90 (47.7)	0.45 (3.60)	⋯ (0.45)	⋯ (⋯)	441. (945.)
[OI] 63.18μm	1057.(1316.)	1862. (2805.)	759. (1593.)	209. (391.)	75.6 (230.)	15.7 (52.6) †	3978. (6335.)‡
[OIII] 88.35μm	1057.(1316.)	762. (1443.)	188. (759.)	100. (209.)†	45.9 (117.) †	4.05 (28.3) †	2007. (3518.) ‡

*Notes: #: total number of AGN inside detectable the SAFARI spectral range; †: outside the SAFARI spectral range;‡: excluding detections outside the SAFARI spectral range.

TABLE 4
NUMBER OF STARBURST GALAXIES DETECTABLE IN A SAFARI SURVEY OF 0.5^2 IN IR LINES AS A FUNCTION OF REDSHIFT AT 5σ (3σ) IN 1 HR. INTEGRATION PER FoV, FOLLOWING GRUPPIONI ET AL. (2011)

line/redshift	0<z<0.75	0.75<z<1.25	1.25<z<1.75	1.75<z<2.25	2.25<z<2.75	2.75<z<4	all redhifts #
PAH(11.25μm)	515. (779.) †	245. (329.) †	270. (373.) †	71.1 (140.)	19.8 (48.2)	2.70 (10.4)	93.6 (199.) ‡
[NeII] 12.81μm	326. (515.) †	212. (284.) †	128. (219.)	48.1 (102.)	11.7 (31.5)	1.35 (5.85)	189. (358.) ‡
[NeIII] 15.55μm	62.1 (115.) †	52.2 (72.0)	29.2 (64.8)	13.0 (32.4)	2.25 (7.20)	0.45 (2.70)	97.1 (179.) ‡
H₂(17.03μm)	26.6 (46.3) †	9.90 (24.8)	6.30 (11.2)	0.90 (4.05)	··· (0.45)	··· (···)	17.1 (40.5) ‡
[SIII] 18.71μm	115. (199.) †	36.4 (72.0)	18.4 (43.6)	7.65 (20.7)	2.25 (7.20)	··· (0.45)	64.7 (144.) ‡
[OIV] 25.89μm	8.10 (15.3)	3.60 (9.90)	3.15 (11.2)	0.90 (1.80)	··· (···)	··· (···)	15.8 (38.2)
[SIII] 33.48μm	199. (326.)	180. (245.)	171. (270.)	71.1 (140.)	31.5 (69.8)	5.85 (18.4)	658. (1069.)
[SiII] 34.81μm	256. (412.)	245. (329.)	270. (373.)	140. (240.)	69.8 (136.)	18.4 (46.4)	999. (1536.)
[OIII] 51.81μm	92.7 (219.)	180. (245.)	171. (321.)	48.1 (140.)	4.05 (19.8)	··· (0.45)	496. (945..)
[NIII] 57.32μm	153. (326.)	52.2 (122.)	18.4 (64.8)	0.45 (4.05)	··· (···)	··· (···)	224. (517.)
[OI] 63.18μm	637. (939.)	329. (459.)	321. (422.)	140. (240.)	31.5 (99.0)	5.85 (18.4) †	1458. (2159.) ‡
[OIII] 88.35μm	637. (939.)	212. (284.)	171. (321.)	71.1 (140.) †	19.8 (48.1) †	1.35 (10.4) †	1020. (1544.) ‡

*Notes: #: total number of AGN inside detectable the SAFARI spectral range; †: outside the SAFARI spectral range;‡: excluding detections outside the SAFARI spectral range.

TABLE 5
TOTAL NUMBER OF GALAXIES DETECTABLE IN A SAFARI SURVEY OF 0.5^2 IN IR LINES AS A FUNCTION OF REDSHIFT AT 5σ (3σ) IN 1 HR. INTEGRATION PER FoV, FOLLOWING VALIANTE ET AL. (2009)

line/redshift	0<z<0.75	0.75<z<1.25	1.25<z<1.75	1.75<z<2.25	2.25<z<2.75	2.75<z<4	all redhifts #
PAH(11.25μm)	3353 (5602) †	2383. (4094.) †	1074. (2743.) †	322. (676.)	91.3 (308.)	4.95 (19.8)	418. (1004.)‡
[NeII] 12.81μm	1114 (1811) †	251. (595.) †	28.8 (136.)	11.7 (49.1)	1.8 (15.8)	··· (···)	42.3 (201.)‡
[NeIII] 15.55μm	850 (1429) †	94.0 (252.)	51.8 (136.)	26.1 (85.1)	7.2 (29.2)	··· (4.95)	179. (507.)‡
H₂(17.03μm)	158 (331) †	4.95 (17.1)	1.35 (7.65)	··· (···)	··· (···)	··· (···)	6.3 (24.8)‡
[SIII] 18.71μm	158 (331) †	4.95 (17.1)	1.35 (7.65)	··· (···)	··· (1.80)	··· (···)	6.3 (26.5)‡
[OIV] 25.89μm	638 (1114)	94.0 (252.)	136. (327.)	49.1 (211.)	15.8 (51.8)	··· (4.95)	938. (1961.)
[SIII] 33.48μm	638 (1114)	251. (327.)	136. (327.)	49.1 (211.)	29.3 (142.)	··· (4.95)	1103. (2678.)
[SiII] 34.81μm	1114 (1811)	879. (1761.)	505. (1074.)	322. (676.)	207. (452.)	9.9 (61.2)	3037. (5835.)
[OIII] 51.81μm	2258 (4010)	879. (1761.)	505. (1512.)	212. (676.)	29.2 (142.)	··· (4.95)	3883. (8106.)
[NIII] 57.32μm	850 (1811)	94.0 (392.)	28.8 (136.)	··· (11.7)	··· (···)	··· (···)	973. (2351.)
[OI] 63.18μm	3353 (4762)	3149. (5211.)	1512. (2743.)	676. (1326.)	207. (639.)	19.8 (61.2) †	8897. (14681.) ‡
[OIII] 88.35μm	3353 (4762)	1263. (2383.)	505. (1512.)	322. (955.) †	142. (307.)†	4.9 (36.0)†	5121. (8657.) ‡

*Notes: #: total number of AGN inside detectable the SAFARI spectral range; †: outside the SAFARI spectral range;‡: excluding detections outside the SAFARI spectral range.

TABLE 6
NUMBER OF GALAXIES DETECTABLE IN A CCAT SURVEY OF 0.5^2 IN IR LINES AS A FUNCTION OF REDSHIFT AT 5σ (3σ) IN 1 HR. INTEGRATION PER FoV, FOLLOWING FRANCESCHINI ET AL. (2010)

line/redshift	0<z<0.75	0.75<z<1.25	1.25<z<1.75	1.75<z<2.25	2.25<z<2.75	2.75<z<4
[OI] 63.18μm	··· (···)	··· (···)	··· (···)	0.27 (3.60) ⋄	··· (0.27) †	··· (0.22)‡
[OIII] 88.35μm	··· (···)	22.2 (67.5) ⋄	1.80 (25.8) †	2.07 (12.1) ‡	86.0 (219.) #	21.1 (67.0) $
[NII] 121.90μm	13.5 (39.0) †	0.22 (0.85) †	0.27 (1.80) ‡	12.1 (59.0) #	3.15 (27.0) $	0.22 (1.53) §
[OI] 145.52μm	0.45 (1.35) †	··· (0.09) ‡	0.86 (3.02) #	··· (0.25) $	··· (···) §	··· (0.72) ¶
[CII] 157.74μm	235. (643.) †	1786. (3951.) #	1314. (1998.) $	517. (1116.) $	219. (603.) §	350. (603.) ¶

*Notes: ⋄: at 200μm band; †: at 230μm band; ‡: at 291μm band; #: at 350μm band; $: at 450μm band; §: at 620μm band; ¶:at 740μm band

TABLE 7

NUMBER OF GALAXIES DETECTABLE IN A CCAT SURVEY OF 0.5^2 IN IR LINES AS A FUNCTION OF REDSHIFT AT 5σ (3σ) IN 1 HR. INTEGRATION PER FOV, FOLLOWING GRUPPIONI ET AL. (2011)

line/redshift	0<z<0.75	0.75<z<1.25	1.25<z<1.75	1.75<z<2.25	2.25<z<2.75	2.75<z<4
[OI] 63.18μm	$\cdots$ ($\cdots$)	$\cdots$ ($\cdots$)	$\cdots$ ($\cdots$)	2.02 (13.7) $\diamond$	0.36 (1.53) $\dagger$	0.22 (1.71) $\ddagger$
[OIII] 88.35μm	$\cdots$ ($\cdots$)	22.1 (53.5) $\diamond$	5.49 (28.6) $\dagger$	7.47 (25.3) $\ddagger$	108. (240.) #	39.7 (118.) \$
[NII] 121.90μm	12.7 (32.5) $\dagger$	0.81 (3.01) $\dagger$	1.53 (5.49) $\ddagger$	25.3 (71.1) #	11.0 (37.9) §	1.71 (6.12) §
[OI] 145.52μm	0.81 (2.02) $\dagger$	$\cdots$ (0.45) $\ddagger$	2.65 (9.85) #	1.00 (3.60) \$	0.13 (0.72) §	0.49 (3.01) ¶
[CII] 157.74μm	172. (432.) $\dagger$	1728. (3262.) #	1498. (2628.) \$	473. (1089.) \$	240. (534.) §	572. (882.) ¶

[*]Notes: $\diamond$: at 200μm band; $\dagger$: at 230μm band; $\ddagger$: at 291μm band; #: at 350μm band; \$: at 450μm band; §: at 620μm band; ¶:at 740μm band

TABLE 8

NUMBER OF GALAXIES DETECTABLE IN A CCAT SURVEY OF 0.5^2 IN IR LINES AS A FUNCTION OF REDSHIFT AT 5σ (3σ) IN 1 HR. INTEGRATION PER FOV, FOLLOWING VALIANTE ET AL. (2009)

line/redshift	0<z<0.75	0.75<z<1.25	1.25<z<1.75	1.75<z<2.25	2.25<z<2.75	2.75<z<4
[OI] 63.18μm	$\cdots$ ($\cdots$)	$\cdots$ ($\cdots$)	$\cdots$ ($\cdots$)	$\cdots$ (26.4) $\diamond$	$\cdots$ (1.94) $\dagger$	$\cdots$ (0.09) $\ddagger$
[OIII] 88.35μm	$\cdots$ ($\cdots$)	17.5 (54.9) $\diamond$	3.69 (28.7) $\dagger$	12.0 (49.5) $\ddagger$	208. (450.) #	36.1 (97.6) \$
[NII] 121.90μm	13.1 (40.5) $\dagger$	0.13 (1.00) $\dagger$	0.13 (3.69) $\ddagger$	49.5 (136.) #	29.2 (91.3) \$	0.09 (4.81) §
[OI] 145.52μm	0.94 (1.44) $\dagger$	$\cdots$ (0.09) $\ddagger$	1.35 (7.65) #	$\cdots$ (3.73) \$	$\cdots$ ($\cdots$) §	$\cdots$ (1.66) ¶
[CII] 157.74μm	231. (639.) $\dagger$	2385. (5211.) #	2061. (3586.) \$	954. (2371.) \$	450. (1215.) §	531. (1075.) ¶

[*]Notes: $\diamond$: at 200μm band; $\dagger$: at 230μm band; $\ddagger$: at 291μm band; #: at 350μm band; \$: at 450μm band; §: at 620μm band; ¶:at 740μm band